



# Immunogenic-cell-killing and immunosuppression-inhibiting nanomedicine

Ying Wang<sup>a,1</sup>, Di Gao<sup>a,1</sup>, Yan Liu<sup>b</sup>, Xiaoqing Guo<sup>a</sup>, Shuojia Chen<sup>a</sup>, Li Zeng<sup>a</sup>, Jinxuan Ma<sup>a</sup>,  
Xingcai Zhang<sup>b,c,\*</sup>, Zhongmin Tian<sup>a,\*\*</sup>, Zhe Yang<sup>a,\*\*\*</sup>

<sup>a</sup> The Key Laboratory of Biomedical Information Engineering of Ministry of Education, School of Life Science and Technology, Xi'an Jiaotong University, Xi'an, 710049, China

<sup>b</sup> John A. Paulson School of Engineering and Applied Sciences, Harvard University, Cambridge, MA, 02138, United States

<sup>c</sup> School of Engineering, Massachusetts Institute of Technology, Cambridge, MA, 02139, United States

## ARTICLE INFO

### Keywords:

Controllable upper critical solution temperature (UCST)  
Immunogenic cell death (ICD)  
Indoleamine 2,3-dioxygenase 1 (IDO1)  
Drug delivery  
Cancer chemoimmunotherapy

## ABSTRACT

Combining chemo-therapeutics with immune checkpoint inhibitors facilitates killing cancer cells and activating the immune system through inhibiting immune escape. However, their treatment effects remain limited due to the compromised accumulation of both drugs and inhibitors in certain tumor tissues. Herein, a new poly (acrylamide-co-acrylonitrile-co-vinylimidazole-co-bis(2-methacryloyl) oxyethyl disulfide) (PAAVB) polymer-based intelligent platform with controllable upper critical solution temperature (UCST) was used for the simultaneous delivery of paclitaxel (PTX) and curcumin (CUR). Additionally, a hyaluronic acid (HA) layer was coated on the surface of PAAVB NPs to target the CD44-overexpressed tumor cells. The proposed nanomedicine demonstrated a gratifying accumulation in tumor tissue and uptake by cancer cells. Then, the acidic microenvironment and high level of glutathione (GSH) in cancer cells could spontaneously decrease the UCST of polymer, leading to the disassembly of the NPs and rapid drug release at body temperature without extra-stimuli. Significantly, the released PTX and CUR could induce the immunogenic cell death (ICD) to promote adaptive anti-tumor immunogenicity and inhibit immunosuppression through suppressing the activity of indoleamine 2,3-dioxygenase 1 (IDO1) enzyme respectively. Therefore, the synergism of this intelligent nanomedicine can suppress primary breast tumor growth and inhibit their lung metastasis.

## 1. Introduction

Blockade of immune checkpoints, as one type of immunotherapies for the treatment of cancer, utilizes inhibitors to overcome the immunosuppression and facilitate the immune system to recognize and attack cancer cells [1–4]. IDO1 is commonly used as an essential checkpoint to defend against a variety of pathogens through mediating tryptophan (Trp) degradation to kynurenine (Kyn) [5–8]. However, overexpression or hyperactivity of IDO1 usually appears in cancer cells and neighboring immune cells [9], leading to the suppression of effector CD8<sup>+</sup> T cells' proliferation and the enhancement of regulatory T cells' suppressive activity [10–13]. IDO1 inhibitors are therefore greatly needed, which have been widely explored and applied in clinical trials, such as Indoximod®, Navoximod®, etc. [6,14–16]. Additionally, some chemotherapeutics have shown powerful abilities in inhibiting the activity of

IDO1. For example, curcumin (CUR), a natural phenolic compound with the anti-cancer ability [17,18], was validated to be anti-inflammatory and anti-oxidant, which also plays a significant role in suppressing enzymatic functions of IDO1 [19,20].

Combined with chemotherapeutics, IDO1 inhibitors can provide an enhanced ability for cancer treatment [21,22]. During synergistic therapy, chemotherapeutics, such as paclitaxel (PTX) and doxorubicin (DOX) can induce immunogenic cell death (ICD) to express or release damage-associated molecular patterns (DAMPs), including calreticulin (CRT), high-mobility group box 1 (HMGB-1), and adenosine triphosphate (ATP) [8,22–29]. These DAMPs can not only increase the immunogenicity of cancer cells but stimulate the immune system to attack tumors, assisting IDO1 inhibitors to enhance the immunotherapeutic effect [30]. So far, a few combinational treatments have been introduced into the clinical trials [31]. However, water solubility and

\* Corresponding author.

\*\* Corresponding author

\*\*\* Corresponding author

E-mail addresses: [xingcai@mit.edu](mailto:xingcai@mit.edu) (X. Zhang), [zmtian@mail.xjtu.edu.cn](mailto:zmtian@mail.xjtu.edu.cn) (Z. Tian), [yangzhe@xjtu.edu.cn](mailto:yangzhe@xjtu.edu.cn) (Z. Yang).

<sup>1</sup> These authors contributed equally to this work.

<https://doi.org/10.1016/j.bioactmat.2020.11.016>

Received 15 September 2020; Received in revised form 6 November 2020; Accepted 6 November 2020

Available online 19 November 2020

2452-199X/© 2020 The Authors. Production and hosting by Elsevier B.V. on behalf of KeAi Communications Co., Ltd. This is an open access article under the CC

BY-NC-ND license (<http://creativecommons.org/licenses/by-nc-nd/4.0/>).

bioavailability of the above-mentioned IDO1 inhibitors and chemo-drugs are compromising, which may reduce their synergistic efficacy [6,32].

Ideally, controlled drug delivery nanosystems should be able to both deliver multiple active drugs at a constant rate over a prolonged period and precisely release them at the target site [33–37]. Accordingly, the bioavailability of drugs can be improved and the risk of side effects can be reduced by incorporating them into nanocarriers. Current UCST studies still possess limitations for the realistic implication that the tissue penetration depth is insufficient and the light is scattered [37]. Thus, it is desirable to prepare a more intelligent drug delivery system for cancer therapy.

The thermo-responsiveness of UCST polymers is predominated mainly by their hydrophobic counter ions, molecular weight, and supramolecular interactions between the polymer side groups [38,39]. Meanwhile, it has been found that endo-trigger stimuli, such as a higher level of GSH and lower pH value in tumor tissue or intracellular organelles, could influence the UCST of the polymer via altering polymer structure [40–44]. For example, redox processes can influence the UCST phase transition of the polymer by changing the structure or molecular weight of the polymer. Beyond that, protonation and deprotonation of functional groups under acidic condition is also an effective approach that can affect the electrostatic interactions and hydrogen bonding of polymers [37]. These endogenous changes for cancer cells that can influence the thermo-response behaviors of polymers have given us inspirations to develop new polymers for smart drug delivery by using environment-controllable UCST phase transition.

In the current paper, a new polymer with controllable UCST, poly

(acrylamide-co-acrylonitrile-co-vinylimidazole-co-bis(2-methacryloyl)oxyethyl disulfide) (PAAVB), was proposed, designed, and synthesized by radical polymerization. Its UCST could be tuned at different pH values and GSH levels. Furthermore, the resultant polymer was utilized to prepare nanoparticles (NPs) for delivering CUR and PTX. To improve the stability and targeting efficiency of NPs, hyaluronic acid-hexadecylamine conjugant (HA-HDA), a cluster determinant 44 (CD44) targeting lipid [45,46], was coated on the surface of PAAVB NPs through the hexadecyl anchors on the hydrophobic core of PAAVB NPs (Fig. 1). When this responsive drug delivery nano-platform was in the systemic circulation, the high UCST (>45 °C) of PAAVB polymer in the physiological environment would make both PTX and CUR entrapped in NPs to avoid the toxic side effects imposed by drug leakage. However, as they arrived at tumor tissue or intracellular organelles (endosome or lysosome), the acidic environment might lead to the protonation of the imidazole group in polymer and enhance electrostatic repulsion. Additionally, the high level of GSH might also break the disulfide bonds and reduce the molecular weight of the PAAVB polymer. Both of them would break the hydrogen bonds by reducing the UCST (<37 °C) of polymer, which might cause the disassembly of PAAVB NPs and accelerate the release of PTX and CUR. The released PTX then could induce the ICD to promote adaptive anti-tumor immunogenicity, where the released CUR could reverse the immunosuppressive tumor environment (ITM) by inhibiting the activity of IDO1. By developing this intelligent nanomedicine in this way, the synergetic effect of it could suppress the primary breast tumor growth as well as their lung metastasis.

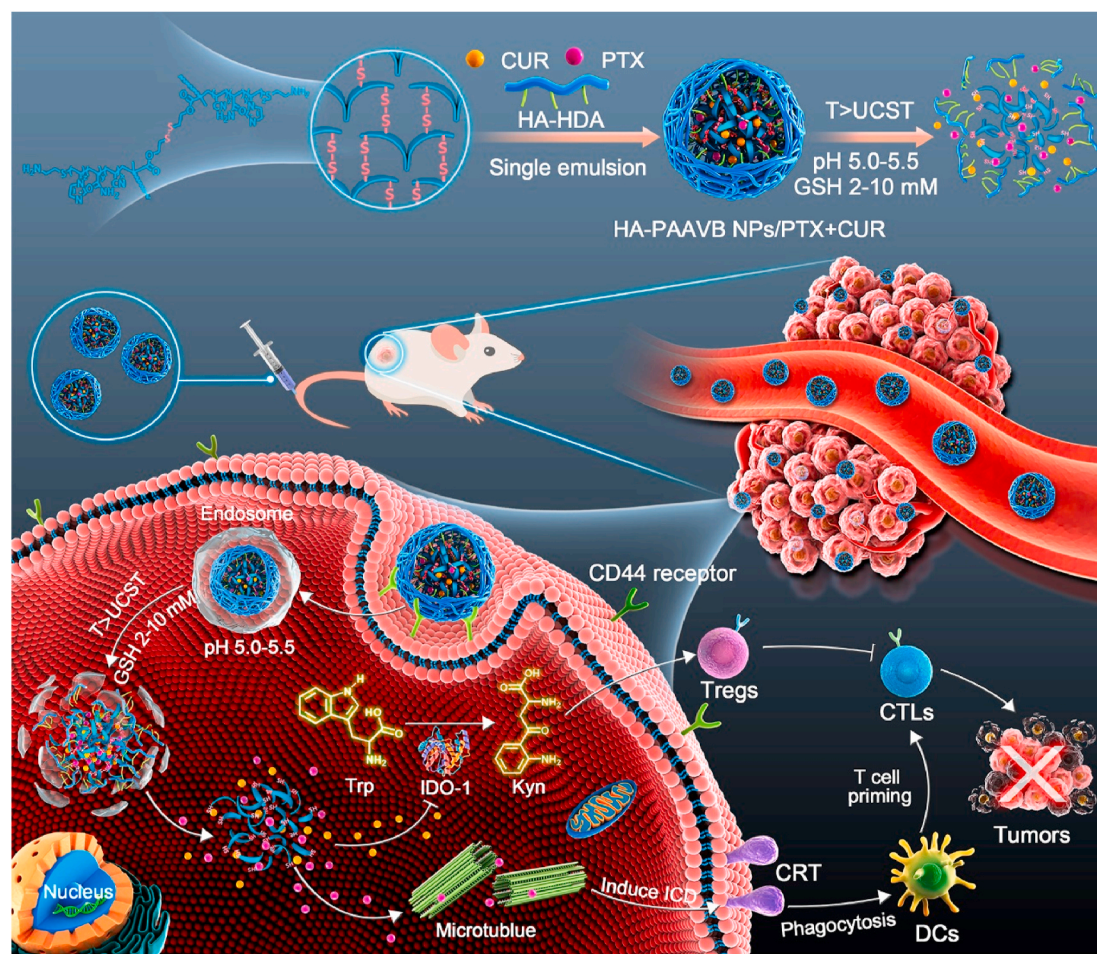


**Fig. 1.** Schematic illustration of the targeted and intelligent nano-platform with controllable UCST for co-delivery of paclitaxel and curcumin, and the mechanistic action of achieving immunogenic cell death and reversing immunosuppression.

## 2. Method

### 2.1. Materials, cells, and animals

1-Vinylimidazole (VIm), acrylonitrile (AN), acrylamide (AAm), 2, 2'-azobisisobutyronitrile (AIBN), bis(2-methacryloyl)oxyethyl disulfide (BMAODS), *N*-(3-dimethylaminopropyl)-*N'*-ethylcarbodiimide hydrochloride (EDC), *N*-hydroxysuccinimide (NHS), Hoechst 33,342, 2-aminoethanethiol hydrochloride (AET·HCl), coumarin 6 (C6), 3-(4,5-dimethyl-2-thiazolyl)-2,5-diphenyl-2H-tetrazolium bromide (MTT) and glutathione (GSH) were obtained from Sigma. DiR was purchased from Biotium Inc. (USA). Hyaluronic acid (HA, 60 kDa) was obtained from Shengqiang Biotech Co., Ltd (China). Curcumin (CUR) and hexadecylamine (HDA) were purchased from TCI Development Co., Ltd (China). Paclitaxel (PTX) was purchased from Shanghai Knowshine Pharmaceuticals Inc. (China). The HMGB1 ELISA kit was purchased from Shanghai Enzyme-linked Biotechnology Co., Ltd. (China).

4T1 cells (murine breast cancer cells), LO2 cells (human liver cells), and HK2 (human renal tubular epithelial cells) were cultured in Dulbecco's Modified Eagle's Medium (DMEM) supplemented with 10% fetal bovine serum (FBS) and 1% penicillin-streptomycin at 37 °C in a humidified environment with 5% CO<sub>2</sub>. All cells were acquired from the Shanghai Cell Bank of the Chinese Academy of Sciences (China).

The protocol for animal experiments was approved by the Animal Experimentation Ethics Committee of Xi'an Jiaotong University. Female balb/c mice (5–6 weeks) were purchased and maintained in the Center for Experimental Animals at Xi'an Jiaotong University Health Science Center. The tumor volume was measured via a serial caliper and estimated using the formula [47]:

$$\text{Volume} = 0.5 \times \text{length} \times (\text{width})^2 \quad (1)$$

### 2.2. Synthesis of PAAVB copolymer

Poly(acrylamide-co-acrylonitrile-co-vinylimidazole-co-bis(2-methacryloyl)oxyethyl disulfide) copolymer (PAAVB) was synthesized using AAm, AN, VIm and BMAODS as monomers, AET·HCl as a chain transfer agent and AIBN as an initiator [37,48]. Briefly, a mixture of AET·HCl (0.141 mmol), AIBN (0.028 mmol), VIm (1.082 mmol), AN (3.788 mmol), AAm (7.034 mmol), and BMAODS (ranging from 0.04 to 0.16 mmol) in 8 mL of anhydrous dimethylformamide (DMF) was added to a 25 mL Schlenk flask. After three cycles of freeze-vacuum-thaw, the resultant mixture was stirred at 65 °C under argon protection for 24 h. Subsequently, the reacted solution was precipitated twice in cool methanol and lyophilized for further use. As a control, poly(acrylamide-co-acrylonitrile-co-vinylimidazole) copolymer (PAAV) was synthesized using a similar procedure except that BMAODS was not added. The <sup>1</sup>H NMR spectra (Agilent Technologies 800/54 premium) and gel permeation chromatography (GPC, Waters) results were used to verify the chemical structures of the polymer (see the supplementary information).

### 2.3. Turbidity measurements of PAAVB copolymer

The copolymers were dispersed in PBS (pH 7.4, 6.8 and 5.5, 0.01 M) containing different concentrations of GSH (0 mM, 10 μM, and 10 mM) at different temperatures, and their turbidity was recorded using a UV-Vis spectrophotometer (Purkinje T6-1610F, China) at a wavelength of 650 nm with a heating rate of 0.5 °C/min. To obtain an accurate UCST value, the value of UCST was calculated by the function of Boltzmann in the nonlinear curve fitting of origin software. The UCST was defined as the temperature at which it reached the half of the changed transmittance [49]. The UCST was defined as the temperature at which the transmittance reached 50%. In addition, the molecular weight of various

polymers after incubation in different buffer solutions was measured using GPC.

### 2.4. Fabrication of HA-PAAVB NPs

Briefly, 0.5 mL of 20 mg/mL PAAVB copolymer DMSO solution was injected into 2 mL of HA-HDA aqueous solution (2 mg/mL) under probe sonication at 14 W for 1 min on ice (Sonics & Materials, VCX500). Then, the resultant emulsion was transferred into a dialysis bag (MWCO 3500 Da) and dialyzed against deionized water overnight. To evaluate the drug-loading properties, cellular uptake and biodistribution of HA-PAAVB NPs, the drugs or the fluorescent dyes-loaded HA-PAAVB NPs were prepared using the same protocol for the fabrication of blank NPs, except that the drugs (0.5 mg PTX and 1 mg CUR) or the fluorescent dyes (0.05 mg coumarin 6 or 0.2 mg DiR) were added to the polymer DMSO solution during the NPs preparation, respectively. Since both PTX, CUR, coumarin 6 (C6), DiR and PAAVB polymer were hydrophobic, the drugs could be encapsulated into the NPs through the hydrophobic interaction between polymers and drugs during the formation of NPs. Afterward, the size distribution and zeta potential of HA-PAAVB NPs were characterized using a dynamic light scattering (DLS) analyzer (NanoBrook 90 Plus, USA). Meanwhile, the morphology of HA-PAAVB NPs was observed using a transmission electron microscope (TEM, JEM-200CX).

To analyze the environment-sensitive behavior of HA-PAAVB NPs, the nanoparticles were incubated in PBS (pH 7.4, 6.8, and 5.5) containing GSH (0 mM, 10 μM, and 10 mM) at 37 °C for 0.5 h followed by measuring their size distribution and morphology, respectively.

### 2.5. Stability of HA-PAAVB NPs

To estimate the stability of HA-PAAVB NPs in the physiological environment, the nanoparticles were incubated in DMEM containing 10% FBS at 37 °C for 48 h. At predetermined intervals, samples were collected and their average size was determined using DLS.

### 2.6. Biocompatibility of HA-PAAVB NPs

To study the biocompatibility of HA-PAAVB NPs, the hemolysis tendency of HA-PAAVB NPs was evaluated. In brief, the erythrocytes at the density of  $1 \times 10^7$  cells/mL were incubated with HA-PAAVB NPs at concentrations ranging from 50 μg/mL to 500 μg/mL at 37 °C for 12 h. Triton X-100 (1%, v/v) solution and PBS (pH 7.4, 0.01 M) were regarded as the positive control and negative control, respectively. Afterward, the suspensions were centrifuged at 2000 rpm for 5 min. The absorbance of hemoglobin at a wavelength of 410 nm in the supernatant was measured with a microplate reader (Tecan M200). Hemolytic activity (%) was calculated using the following formula:

$$\text{Hemolysis (\%)} = (A_{\text{Sample}} - A_{\text{PBS}}) / (A_{\text{Triton}} - A_{\text{PBS}}) \times 100\% \quad (2)$$

where  $A_{\text{Sample}}$ ,  $A_{\text{PBS}}$ ,  $A_{\text{Triton}}$  represent the absorbance intensity of hemoglobin in HA-PAAVB NPs, PBS, and Triton X-100 groups, respectively.

Besides that, LO2 and HK2 cells were also incubated with HA-PAAVB NPs at different concentrations (50–500 μg/mL) for 48 h followed by measuring the cell viability by MTT assay to further evaluate their biocompatibility and cytotoxicity.

### 2.7. Cellular uptake

To study the targeting ability of HA-PAAVB NPs, the fluorescent dye C6 was encapsulated in the nanoparticles as above described, and the resultant C6-loaded NPs were incubated with 4T1 cells for 4 h. The blank HA-PAAVB NPs was also incubated with 4T1 cells for 4 h. In addition, a competitive inhibition experiment was also performed. 4T1 cells were pre-incubated with or without 10 mg/mL of HA for 1 h. Subsequently,

the resultant cells were treated with HA-PAAVB NPs/C6 for 4 h. Then the cells were washed three times with PBS and harvested. And the intracellular fluorescence intensity of each group was quantitatively detected by flow cytometry (Becton Dickinson, San Jose) at an excitation wavelength of 488 nm. Besides, the cells with the same treatment were also stained with Hoechst 33,342 (10 µg/mL), and the intracellular distribution of NPs was directly visualized using Confocal Laser Scanning Microscopy (CLSM, Leica TCS SP8 STED 3X).

## 2.8. Measurement of PTX and CUR contents in nanoparticles

The content of PTX and CUR encapsulated in nanoparticles was determined by High Performance Liquid Chromatography (HPLC) using a C18 column (25 mm × 4.6 mm, 5 µm) on Agilent 1100 system. The column was eluted using a mixture of acetonitrile and water (60:40, v/v) at the flow rate of 1.0 mL/min at 30 °C. The content of PTX and CUR was monitored at 228 nm and 460 nm with a UV detector, respectively. The drug loading and entrapment efficiency of HA-PAAVB NPs/PTX + CUR were calculated using the following equations:

$$\text{Drug loading (\%)} = \text{drug amount in NPs} / \text{mass of NPs} \times 100\% \quad (3)$$

$$\text{Entrapment efficiency (\%)} = \text{drug amount in NPs} / \text{amount of drug used} \times 100\% \quad (4)$$

## 2.9. In vitro drug release profiles

To investigate *in vitro* drug release profiles, HA-PAAVB NPs were added into dialysis bags (MWCO:14 kDa), and then immersed in PBS (pH 7.4, 6.8 and 5.5, 0.01 M) containing different concentrations of GSH (0 mM, 10 µM and 10 mM) under shaking (150 rpm) at 37 °C. At pre-determined time intervals, the external 4 mL of PBS was removed and the dialysate was replenished with the same volume of fresh PBS. The amount of released PTX and CUR was also measured using the protocol as above described.

## 2.10. Inhibition of breast cancer cell proliferation

Briefly, 4T1 cells at a density of  $5 \times 10^3$  cells/well were seeded in 96-well plates overnight. Then, the medium was removed and replaced by a fresh medium containing various drug formulations. After 48 h of incubation, the cell viability was measured using MTT assay to evaluate the cytotoxicity of different drug formulations on 4T1 cells [50,51].

In addition, immunogenic cell death (ICD) induced by different drug formulations were also evaluated.  $3 \times 10^6$  4T1 cells were treated with different drug formulations at a concentration of PTX (5 µg/mL) and CUR (11 µg/mL) for 48 h. Afterward, 4T1 cells were harvested to evaluate the CRT expression using Western blot. Besides, the supernatant media were also collected to measure the concentration of released high mobility group protein B1 (HMGB1) using enzyme linked immunosorbent assay (ELISA).

To further confirm whether the dead cells induced by the treatment of different drug formulations could activate the immune system,  $1 \times 10^6$  dead 4T1 cells were injected subcutaneously into the left flank of balb/c mice (n = 5) on days 0 and 7. One week later,  $1 \times 10^6$  live 4T1 cells were injected on the right flank of mice. Then the volume of right tumors in each group was measured every day during the experiment. At the end of the experiment, the mice were sacrificed and their tumors were collected for IHC analysis.

## 2.11. IDO1 cellular activity test

The inhibitory effect of different drug formulations on IDO1 activity was evaluated by measuring kynurenine (Kyn) content after treatments, which is one of the important metabolites of tryptophan [13,52]. In

brief, after 4T1 cells were pre-treated with Trp (100 µM) overnight, IFN-γ (0.1 µg/mL) and various drug formulations at concentration of PTX (0.9 µg/mL) and CUR (2 µg/mL) were also added. After 48 h of incubation, the medium was centrifuged and the supernatants were collected. Then 50 µL of 30% TCA was added into supernatants for protein precipitation. Afterward, Kyn was determined using HPLC. The column was eluted using a mixture of acetonitrile and water (30:70, v/v) at the flow rate of 1.0 mL/min at 30 °C, and the content of Kyn and Trp was monitored at 360 nm and 280 nm with a UV detector, respectively. In addition, the IDO1 expression level of 4T1 cells after the same treatments as described above were also detected using western blotting.

## 2.12. Bio-distribution of HA-PAAVB NPs in tumor-bearing mice

To examine the bio-distribution of HA-PAAVB NPs in 4T1 tumor-bearing mice, the near-infrared fluorescent dye, DiR, was encapsulated into HA-PAAVB NPs. When the volume of the subcutaneous 4T1 tumor reached 200–300 mm<sup>3</sup>, eight mice were randomly divided into two groups. Free DiR and HA-PAAVB NPs/DiR were intravenously administered into mice, respectively (the dosage of DiR was calculated as 0.35 mg per kg mouse). At pre-determined intervals (2, 4, 8, 10, and 24 h), the fluorescent images were captured using an *in vivo* imaging system (IVISs Lumina XR Series III, PerkinElmer). Then the mice were sacrificed and major tissues (heart, liver, spleen, lung, kidney, and tumor) were harvested for *ex-vivo* imaging.

## 2.13. In vivo therapeutic efficacy

To study the *in vivo* anticancer effect, the balb/c mice bearing subcutaneous 4T1 tumors were established. When the tumor volume approximated to 150 mm<sup>3</sup>, the 4T1 tumor-bearing mice were randomly subdivided into five groups (n = 10 per group). Then different drug formulations were intravenously injected into mice on days of 0, 2, 4, and 6 at doses of PTX (3 mg/kg) and CUR (6.6 mg/kg), respectively. Tumor volumes and mice weights were measured every day during the experiment. The tumor growth inhibition (TGI) was calculated by the following equation:  $\text{TGI} = (1 - (\text{Mean tumor volume of treatment group}) / (\text{Mean tumor volume of 0.9\% NaCl group})) \times 100\%$ , where the tumor volume was calculated on the same day [53,54]. On day 18, five mice from each group were sacrificed, and their tumors were harvested and stained using hematoxylin and eosin (H&E). The survival rates of the remaining mice were monitored.

For immunoassay, the single-cell suspension from the harvested tumor tissue was utilized to detect the cellular activity of the IDO1 enzyme, the protocol of which is similar to the above described. In addition, the percentage of CD3<sup>+</sup>CD8<sup>+</sup> and CD3<sup>+</sup>CD4<sup>+</sup> cells were also evaluated using flow cytometry. Briefly, the eviscerated tumor tissues were cut into small pieces, followed by digestion in collagenase type I (1 mg/mL) for 4 h at 37 °C. The digested tissues were meshed twice through a 200-mesh sieve, then centrifuged at 1500 rpm for 5 min to collect the cell pellet. To block nonspecific binding, cell suspensions were incubated with blocking fluid for 30 min. Multiparameter staining was performed by utilizing different combinations of fluorophore-conjugated antibodies for 40 min at 4 °C. The following immune cell subpopulations were investigated, using multichannel gating: CD8<sup>+</sup> T cells (CD3<sup>+</sup>CD4<sup>+</sup>CD8<sup>+</sup>), CD4<sup>+</sup> T cells (CD3<sup>+</sup>CD4<sup>+</sup>CD8<sup>-</sup>), and Tregs (CD4<sup>+</sup>CD25<sup>+</sup>CD127<sup>-</sup>).

Furthermore, the biosafety of free drugs and drug-loaded NPs were also estimated. In brief, the major organs from mice treated with different drug formulations were harvested and stained using H&E. Additionally, blood was also collected for the routine blood examination and the measurement of aspartate transaminase (AST), creatinine (CRE), alanine aminotransferase (ALT), and urea nitrogen (BUN). Meanwhile, the metabolomics of liver and kidney tissues was also analyzed by gas chromatography-mass spectrometry (GC-MS). In brief, the extraction buffer (methanol/water/chloroform = 2.5:1:1) was added to the liver

and kidney tissues of each mouse according to the ratio 1:10 (w/v). After being stored at  $-80^{\circ}\text{C}$  overnight, the samples were thawed on ice and centrifuged at 12,000 g at  $4^{\circ}\text{C}$  for 10 min. The supernatant (0.14 mL) was transferred to a 2 mL vial for vacuum freeze-drying, and then 50  $\mu\text{L}$  of methoxyamine hydrochloride was added to the freeze-dried sample to react at  $37^{\circ}\text{C}$  for 60 min. After that, 50  $\mu\text{L}$  of N,O-bis(trimethylsilyl)-trifluoroacetamide (BSTFA) was added to the above mixture and incubated at  $60^{\circ}\text{C}$  for 60 min. The metabolites in liver and kidney tissues were determined by an Agilent 7890A gas chromatograph and a 5975C mass spectrometer (Agilent Technologies, Wilmington, DE). In addition, the differential metabolites were identified using the Mann-Whitney-Wilcoxon method [55,56].

#### 2.14. Inhibition of cell migration

Wound-healing assay and transwell assay were used to measure the inhibitory effect of HA-PAAVB NPs/PTX + CUR on 4T1 cell migration. For the wound-healing assay, 4T1 cells at a density of  $3 \times 10^5$  cells/well were seeded in a 24-well plate, and a sterile pipette was used to draw the lines in each well. Then the culture medium was replaced by a fresh medium containing different drug formulations. Following 24 h of treatment, the migration distance was observed and measured using an inverted microscope (Olympus IX53).

For transwell assay, 4T1 cells were seeded in a serum-free medium containing different drug formulations in the apical chamber. Subsequently, the apical chambers were placed in basolateral chambers with the medium containing 50% FBS. After 24 h of incubation, the non-migrated cells in the apical chamber were removed. The migrated cells were stained with 0.1% crystal violet and photographed using an

inverted microscope. Finally, the stained cells were decolorized with 30% acetic acid, and the absorbance of decolorization solution at 540 nm wavelength was measured using a microplate reader (Tecan M200) to quantitatively estimate the migration rate.

#### 2.15. Inhibitor effect on lung metastasis of breast cancer cells

Briefly,  $1 \times 10^5$  4T1 cells were injected into balb/c mice followed by the treatment of different drug formulations at doses of PTX (3 mg/kg) and CUR (6.6 mg/kg) on day of 0, 3, and 6. On the day of 18, the mice were sacrificed, and their lungs were harvested and stained with Bouin's solution to photograph and quantify the number of metastatic nodules. In addition, the harvested lungs were also stained using hematoxylin and eosin (H&E) to further evaluate the inhibitor effect of different drug formulations on lung metastasis of breast cancer cells.

#### 2.16. Statistical analysis

All of the data are reported as the means  $\pm$  standard deviations from at least three repeated experiments. Statistical analyses were performed using a two-sided Student's t-test [57]. A P-value of 0.05 or less was considered to be statistically significant.

### 3. Results

#### 3.1. Synthesis of PAAVB copolymer

Poly (acrylamide-co-acrylonitrile-co-vinylimidazole-co-bis(2-methacryloyl) oxyethyl disulfide) copolymer (PAAVB) was synthesized

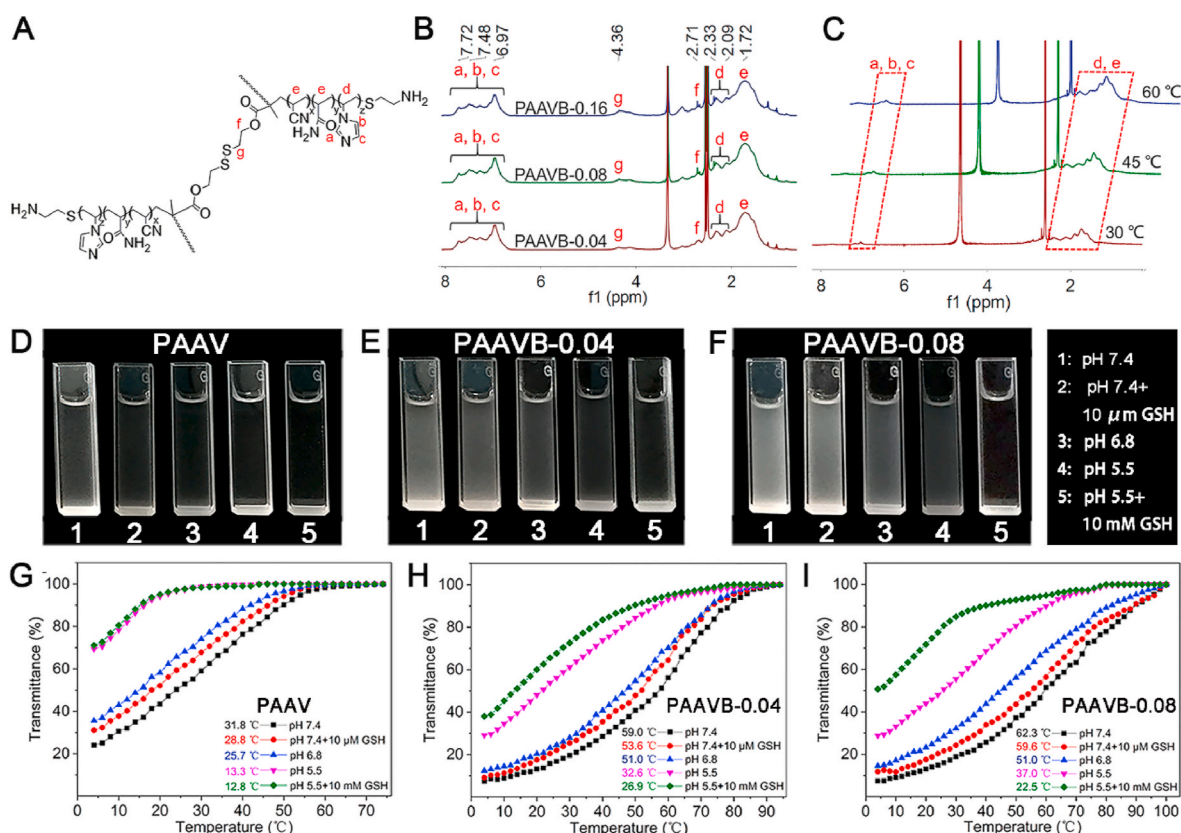


**Fig. 2.** (A) Structure of PAAVB copolymer. (B)  $^1\text{H}$  NMR spectra of PAAVB-0.04, PAAVB-0.08 and PAAVB-0.16 copolymer in  $\text{DMSO}-d_6$ , respectively. (C) Variable temperature  $^1\text{H}$  NMR spectra of PAAVB-0.08 in  $\text{D}_2\text{O}$ . (D–F) Turbidity images of the PAAV, PAAVB-0.04 and PAAVB-0.08 copolymer aqueous solution in various conditions (1: pH 7.4, 2: pH 7.4 with 10  $\mu\text{M}$  GSH, 3: pH 6.8, 4: pH 5.5, 5: pH 5.5 with 10 mM GSH) at 37  $^{\circ}\text{C}$ . (G–I) Turbidity heating profiles of the PAAV, PAAVB-0.04 and PAAVB-0.08 copolymer solutions (0.5 mg/mL) in PBS (pH 7.4, 6.8 and 5.5) containing different concentrations of GSH (0 mM, 10  $\mu\text{M}$  and 10 mM).

through radical polymerization of AAm, AN, VIm and BMAODS (Fig. S1). To investigate the impact of molecular weight and the degree of cross-linking on UCST, the polymers (noted as PAAVB-0.04, PAAVB-0.08, and PAAVB-0.16) were functionalized by adding different molar amounts of BMAODS (0.04, 0.08, and 0.16 mmol) during polymerization. Meanwhile, poly (acrylamide-co-acrylonitrile-co-vinylimidazole) copolymer (PAAV) without BMAODS was synthesized as control. In  $^1\text{H}$  NMR spectra (Fig. 2A–B), the characteristic resonances of PAAVB copolymer are shown as following:  $^1\text{H}$  NMR (400 MHz, DMSO- $d_6$ )  $\delta$  (ppm): 6.97–7.72 (m, imidazole), 1.72–2.33 (m,  $-\text{CH}_2-$  in -AAm-, -AN- and -VIm-), 2.71 ( $-\text{S}-\text{CH}_2-\text{CH}_2-\text{O}-$ ) and 4.36 ( $-\text{S}-\text{CH}_2-\text{CH}_2-\text{O}-$ ). The molecular weights of them were also measured by GPC. Table S1 shows that the molecular weight of PAAVB gradually increased due to the increase of crosslinking degree, which was induced by increasing the BMAODS ratio in the copolymer.

Next, the thermo-sensitivity of PAAVB copolymer was evaluated by measuring the temperature-dependent  $^1\text{H}$  NMR spectra in  $\text{D}_2\text{O}$ . As shown in Fig. 2C, the relative peak integrals of methylene in PAAVB-0.08 copolymer's backbone gradually increased with the elevation of temperature from 30 °C to 60 °C, implying that the enhanced hydration of the relatively hydrophobic segment might occur. It also indicated that the hydrophobic core region of the copolymer in aqueous solution was exposed to the aqueous environment and hydrolyzed in  $\text{D}_2\text{O}$  under high-temperature. Meanwhile, the phase transition of different polymer solutions was recorded under different temperatures. In Fig. S2, the PAAV, PAAVB-0.04, and PAAVB-0.08 were opaque at low temperature, whereas turning to transparency with the temperature being elevated, indicating that these polymers were thermo-sensitive and the higher temperature could break the hydrogen bonds among polymer chains. However, when the molar amounts of BMAODS increased to 0.16 mmol, the PAAVB polymer was not able to disperse in an aqueous solution even in boiling water, thus it was not suitable to apply PAAVB-0.16 in biomedicine. As shown in Fig. 2D–F, we found that the acidic environment with a high GSH level could facilitate the phase transition at 37 °C. To further validate this observation, UCST of different polymers under various conditions was measured through turbidity determination. In Fig. 2G, the UCST of PAAV copolymer was consistently lower than 37 °C in all conditions, which was probably due to its lower molecular weight and weaker intermolecular interactions. The Gibbs energy of dissolution turned positive at temperatures that were lower than the cloud point ( $T_{\text{CP}}$ ) of a UCST polymer, and  $T_{\text{CP}}$  of UCST polymer was relative to  $\Delta H$  and  $\Delta S$  when the value of  $\Delta G$  was zero, which was calculated using the following formulation [38]:

$$T_{\text{CP}} = \Delta H / \Delta S \quad (5)$$

In general, the entropy of polymers mixing was much lower than that for small molecules, and the increase in the molecular weight resulted in the reduction of the entropy of mixing even further. Thus, the molecular weight exhibited a strong influence on the polymer's UCST. Plus, the disulfide-cross-linked PAAVB copolymer possessed higher UCST under the same condition on account of its higher molecular weight. For instance, the UCST of PAAVB-0.04 (59.0 °C) and PAAVB-0.08 (62.3 °C) were obviously higher than that of PAAV (31.8 °C) polymer at physiological condition (pH 7.4) (Fig. 2H–I). The stimuli-responsive properties of UCST for these polymers were also explored. When the PAAVB copolymer was incubated in an acidic solution or solution containing GSH at high concentration, the UCST of PAAVB rapidly decreased. For example, the UCST of PAAVB-0.08 significantly decreased to 51.0 °C in pH 6.8 and 37.0 °C in pH 5.5, respectively. Particularly, as the PAAVB-0.08 polymer was dispersed in pH 5.5 aqueous solution with 10 mM GSH, its UCST further dramatically declined to 22.5 °C. The reason for this phenomenon could be the protonation of the imidazole group in the VIm fragments and cleavage of disulfide in the BMAODS. Once being protonated in an acidic environment, the imidazole groups would be positively charged [58]. The intermolecular electrostatic repulsion

could overrule the weaker hydrogen bonds followed by the disintegration of copolymers, which could finally lead to the reduction of UCST of polymers. In addition, the molecular weight of PAAVB copolymer treated with 10 mM of GSH markedly decreased, which might also lead to the reduction of UCST. Overall, PAAVB copolymer possesses changeable UCST that can be controlled by pH and GSH. Especially for PAAVB-0.08 copolymer, its UCST is more sensitive to environmental change. Thus, PAAVB-0.08 was chosen to prepare the carriers for drug delivery and controlled release in the subsequent studies.

### 3.2. Characterization of blank HA-PAAVB NPs

HA-PAAVB NPs were fabricated using a modified emulsification technique. Due to the amphipathy of HA-HDA, the HA-HDA could attach to the surface of hydrophobic PAAVB NPs cores through the hexadecyl anchors to construct the core-shell NPs. A similar structure of NPs was also reported in our previous studies [45,59,60]. The size and zeta potential of NPs were measured by DLS, which were 154.0 nm and  $-27.3$  mV, respectively. The TEM image showed that the morphology of NPs was spherical in shape (Fig. S3A). To examine the effects of temperature on the size of nanoparticles, the size distribution of blank HA-PAAVB NPs after incubated at different temperatures (25 °C, 37 °C and 43 °C) were measured using DLS, the results were showed in Fig. S3B. Compared to the size of NPs incubated at 25 °C (150 nm), the size of HA-PAAVB NPs incubated at 37 °C and 43 °C increased to 222 nm and 273 nm, respectively, which might be due to the cleavage of part of intermolecular hydrogen bonds with the increment of temperature. Besides, we also studied the stability of HA-PAAVB NPs in PBS containing 10% FBS at 37 °C (Fig. S3C), the results of which showed that HA-PAAVB NPs could still maintain 50–300 nm, indicating that this NP would maintain their stability in the physiological condition *in vivo*.

To evaluate *in vitro* compatibility of HA-PAAVB NPs, their hemolysis activity was measured by incubating NPs with red blood cells. As shown in Fig. S4A, HA-PAAVB NPs exhibited very low hemolysis activity ( $<1.2\%$ ) at various concentrations (50–500  $\mu\text{g}/\text{mL}$ ), indicating that the NPs had excellent hemocompatibility. HA-PAAVB NPs were also incubated with LO2 cells and HK2 cells to assess the potential cytotoxicity on normal cells. As shown in Fig. S4B, there was no significant cytotoxicity on HK2 and LO2 cells, even at the NPs concentration of 500  $\mu\text{g}/\text{mL}$  after 48 h of co-incubation. This behavior indicated that HA-PAAVB NPs could achieve well *in vitro* compatibility, which is one of the basic prerequisites for drug carriers.

### 3.3. Characterization of drug-loaded HA-PAAVB NPs

Drug-loaded HA-PAAVB NPs, including both single drug-loaded NPs (HA-PAAVB NPs/PTX and HA-PAAVB NPs/CUR) and dual drug-loaded NPs (HA-PAAVB NPs/PTX + CUR), were also prepared using the same method and characterized from different aspects. As shown in Fig. 3A, the size of drug-loaded HA-PAAVB NPs ranged from 195 nm to 270 nm with a narrow distribution, and their surface zeta potential was negative ranging from  $-43$  mV to  $-23$  mV. The drug loading of PTX and CUR in the HA-PAAVB NPs/PTX + CUR group was 15.5  $\mu\text{g}/\text{mg}$  and 35.5  $\mu\text{g}/\text{mg}$  of NPs, respectively. In addition, the entrapment efficiencies of them were also computed, which were 27.9% and 32.0%. These results demonstrate that HA-PAAVB NPs have great potential for drug delivery, which is attributed to their good drug loading capacity.

Subsequently, the impact of controllable UCST on drug release was analyzed by measuring the drug release profiles at different conditions. As depicted in Fig. 2B–C, no more than 50% of PTX and 16.5% of CUR were released from HA-PAAVB NPs at pH 7.4 after 72 h. It was also found that extracellular GSH concentration (2–10  $\mu\text{M}$ ) did not substantially impact their drug release in favor of avoiding drug leakage during circulation. However, once the drug-loaded NPs were incubated in acidic conditions (pH 6.8 and pH 5.5) or the solution containing GSH at a high level (10 mM), their drug release was significantly accelerated.

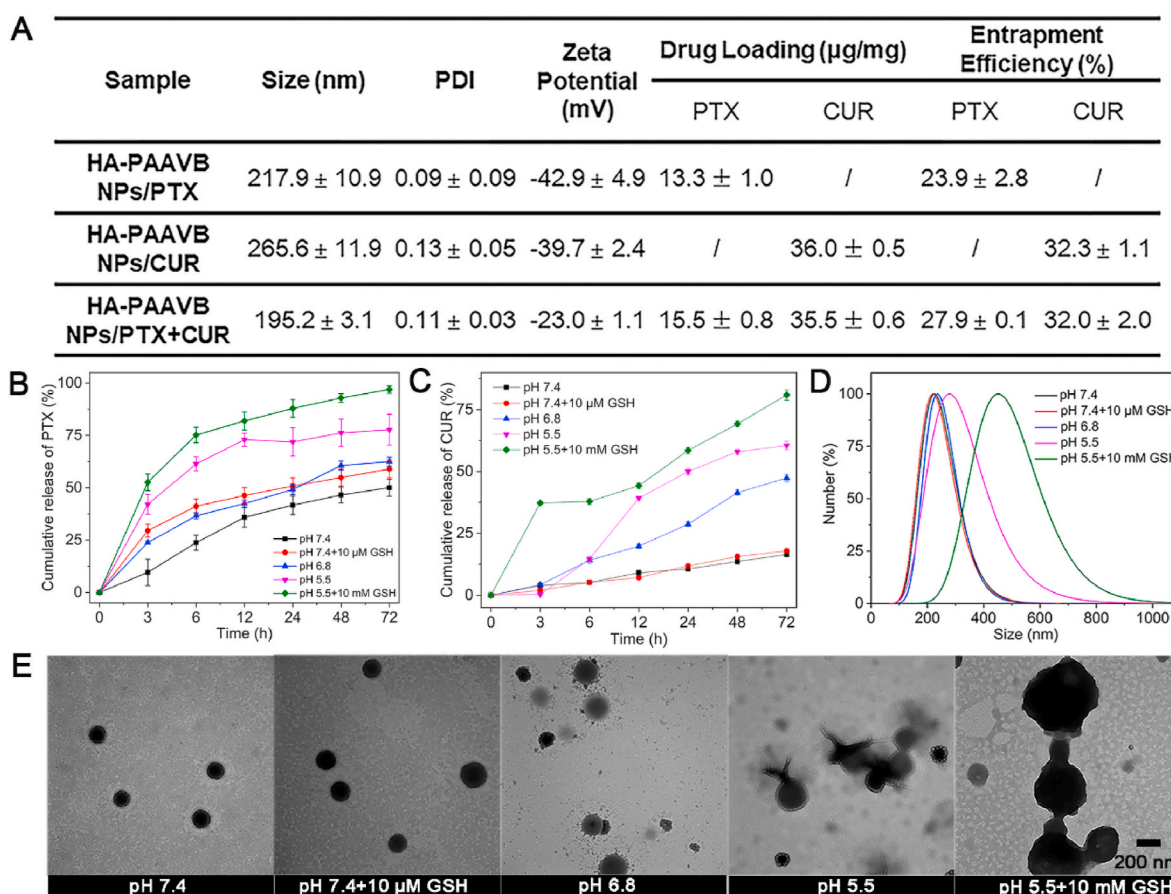


**Fig. 3.** (A) Characterization of PTX- or CUR-loaded HA-PAAVB NPs. (B–C) The cumulative release of PTX and CUR from HA-PAAVB NPs in PBS (pH 7.4, 6.8 and 5.5) containing different concentrations of GSH (0 mM, 10  $\mu\text{M}$  and 10 mM) at 37  $^{\circ}\text{C}$ , respectively. (D) Size distribution and (E) TEM images of HA-PAAVB NPs after incubated in PBS (pH 7.4, 6.8 and 5.5) containing different concentrations of GSH (0 mM, 10  $\mu\text{M}$  and 10 mM). (n = 3).

Especially in the solution at pH 5.5 with 10 mM GSH, 82% of PTX and 44% of CUR were released at the first 12 h of incubation, and more than 97% of PTX and 81% of CUR were released at the end of the experiment. The changeable UCST of PAAVB polymer might be responsible for this phenomenon. Since the UCST of PAAVB could reduce to below 37  $^{\circ}\text{C}$  in an acidic environment containing a high level of GSH, PAAVB NPs could disassemble and achieve the rapid drug release at 37  $^{\circ}\text{C}$ . To verify this hypothesis, the size distribution and morphology of HA-PAAVB NPs after they had been incubated in different solutions at 37  $^{\circ}\text{C}$  were measured using DLS and TEM (Fig. 2D–E). As expected, the size of NPs increased when the pH values dropped from 7.4 to 5.5. In addition, the size of NPs at pH 5.5 with 10 mM GSH increased to 500 nm, and some of them even were distributed in the range of 800–1000 nm, indicating that the decreased UCST at this condition could facilitate the disintegration of HA-PAAVB NPs as well as their drug release. The molecular weight distribution of PAAVB-0.08 after being incubated in PBS (pH 7.4, 6.8, and 5.5) that contained different concentrations of GSH (0 mM, 10  $\mu\text{M}$ , and 10 mM) also could validate this hypothesis (Fig. S5).

### 3.4. Cellular uptake and intracellular distribution of HA-PAAVB NPs

Hyaluronic acid (HA) is a natural, biodegradable, and biocompatible polymer that can be used to targeted CD44 receptors overexpressed on various cancer cells [59,61]. Thus, to test whether HA modification is able to mediate more HA-PAAVB NPs internalizing into CD44 positive cells, the 4T1 cells with a high expression level of CD44 were chosen as the cell model to incubate with C6-loaded HA-PAAVB NPs [46]. In Fig. S6A, it is shown that untreated cells almost had no fluorescence. In addition, the results obtained from the mean fluorescence intensity

(MFI) showed the group pre-incubated with excess HA decreased by 72.8% compared to the group without HA pretreatment (Fig. S6B). Similar results were also observed in CLSM images (Fig. S6C). Therefore, it is convincing that HA-PAAVB NPs possessed excellent targeting capacity to CD44 positive cells, and the interaction between HA and CD44 could also promote the CD44-mediated endocytosis of HA-PAAVB NPs.

### 3.5. *In vitro* antitumor activity of different drug formulations

As shown in Fig. 4A, the drug-loaded HA-PAAVB NPs showed severe toxicity towards 4T1 cells in comparison to the free drug formulations. Especially for the HA-PAAVB NPs/PTX + CUR group, its inhibitor effect against 4T1 cells was better than that of other groups at all concentrations, demonstrating its excellent capacity to suppress cell growth from the synergistic effect of PTX and CUR. The synergistic effect was further evaluated by calculating the combination index (CI) with the following formula [62]:

$$\text{CI} = D_1/D_{1s} + D_2/D_{2s} \quad (6)$$

where  $D_1$  and  $D_2$  are the  $\text{IC}_{50}$  values of PTX ( $0.0369 \pm 0.0004 \mu\text{g}/\text{mL}$ ) and CUR ( $0.08076 \pm 0.0009 \mu\text{g}/\text{mL}$ ) in HA-PAAVB NPs/PTX + CUR group, and  $D_{1s}$  and  $D_{2s}$  are the  $\text{IC}_{50}$  values of PTX ( $0.24707 \pm 0.0161 \mu\text{g}/\text{mL}$ ) and CUR ( $0.5352 \pm 0.0293 \mu\text{g}/\text{mL}$ ) in HA-PAAVB NPs/PTX and HA-PAAVB NPs/CUR groups, respectively (Table S2). CI values were lower than 1 indicating synergism, thus, the CI value of HA-PAAVB NPs/PTX + CUR NPs was 0.3, which could confirm that this drug formulation could be conducive for combining PTX and CUR to achieve the synergistic therapeutic efficacy.

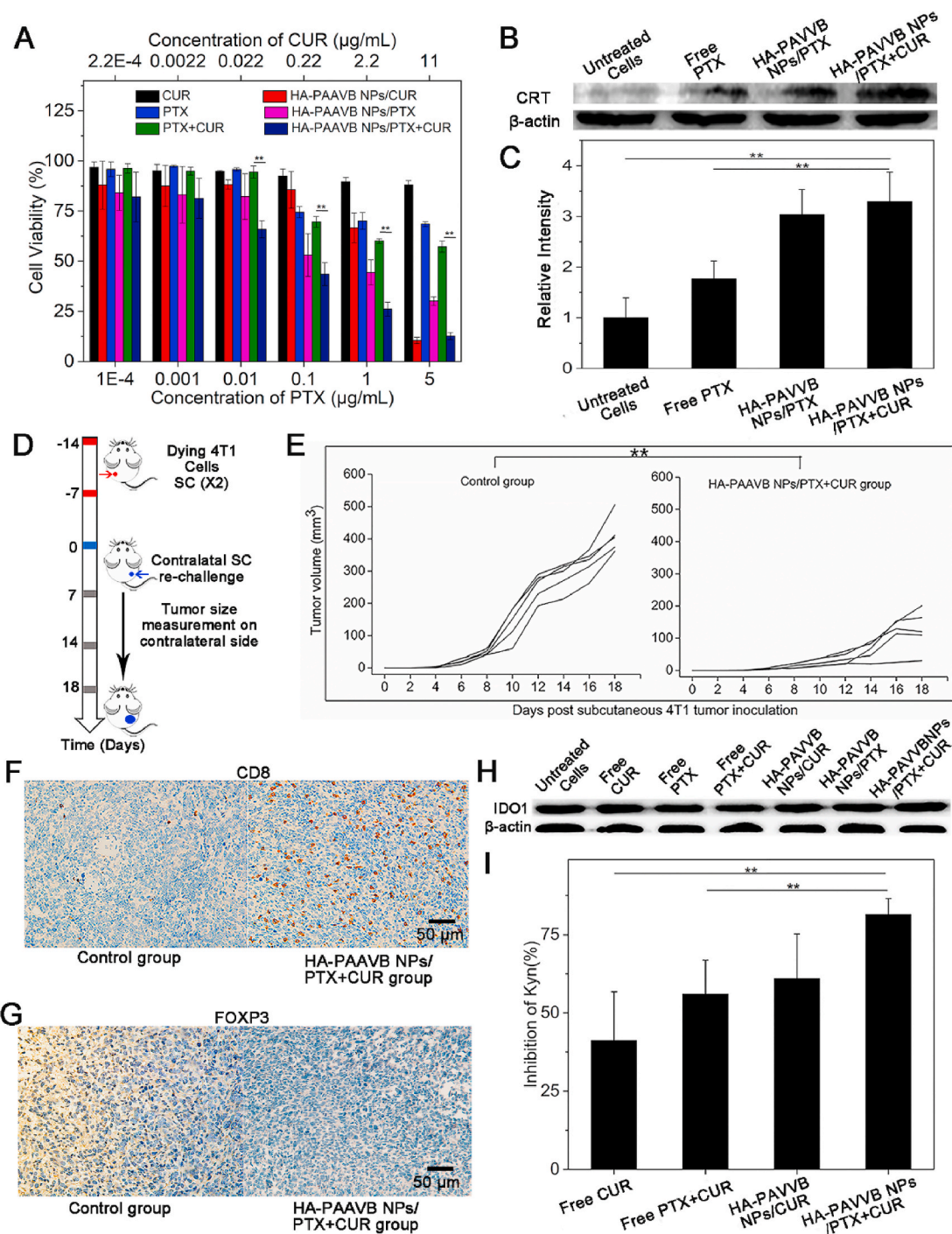


**Fig. 4.** (A) The viability of 4T1 cells incubated with different drug formulations at varying concentrations ( $n = 6$ ). (B) The CRT expression of the 4T1 cells treated with different drug formulations and (C) quantitative analysis of the western blotting bands using ImageJ. Relative intensity was quantified after normalization to untreated cells. (D) Treatment schedule of animal vaccination. (E) The growth of the tumors in animals with or without vaccinated by dying tumor 4T1 cells treated with HA-PAAVB NPs/PTX + CUR ( $n = 5$ ). IHC staining for (F) CD8 and (G) FOXP3 in tumor from animals with or without vaccinated by dying tumor 4T1 cells treated with HA-PAAVB NPs/PTX + CUR. (H) The IDO1 expression of 4T1 cells treated with varying drug formulations. (I) The inhibition rate of Kyn production of the 4T1 cells after treated with different drug formulations for 48 h ( $n = 3$ ).

### 3.6. Immunomodulatory therapy of HA-PAAVB NPs/PTX + CUR

The immunomodulatory ability of HA-PAAVB NPs/PTX + CUR is the focus of our attention, thus, induction of ICD response and inhibition of IDO1 cellular activity was also tested in this study. As shown in Fig. 4B–C, CRT (a hallmark of ICD) in 4T1 cells without treatment was only expressed slightly. However, the treatment containing PTX obviously facilitated the CRT expression in 4T1 cells, especially for HA-

PAAVB NPs/PTX + CUR, there was a 3.29-fold increment than the group of untreated cells. Moreover, we also measured another hallmark of ICD (HMGB1) to demonstrate the occurrence of ICD. As shown in Fig. S7, the level of released HMGB1 also significantly increased after the treatments of drug formulations containing PTX. Especially for the HA-PAAVB NPs/PTX + CUR group, there was a 1.14-fold increment than the group of untreated cells. The above results indicated that the treatment of HA-PAAVB NPs/PTX + CUR could effectively induce ICD in

4T1 cells.

To further investigate the ICD that could be induced by HA-PAAVB NPs/PTX + CUR, the *in vivo* vaccination response was also performed (Fig. 4D). As shown in Fig. 4E, when the living 4T1 cells were subcutaneously injected into the flank of balb/c mice pre-treated with dying tumor cells killed by HA-PAAVB NPs/PTX + CUR, the tumor tissue was formed and grew more slowly than the control group. At the end of the experiment, the tumor tissues in all groups were harvested for immunohistochemistry (IHC), the results of which indicated the increased tumor staining for CD8<sup>+</sup> T cells in parallel with the decreased Tregs (Foxp3<sup>+</sup>) component in animals vaccinated with HA-PAAVB NPs/PTX + CUR-treated cells (Fig. 4F–G and Fig. S8A and B). In addition, we also measured other factors, such as IFN- $\gamma$  and Granzyme B. In Fig. S9A and B, the enhanced level of Granzyme B and IFN- $\gamma$  in HA-PAAVB NPs/PTX + CUR group could also reflect the positive immune effect and enhance immunity against cancer cells. Based on these results, we believed that the treatment of HA-PAAVB NPs/PTX + CUR could effectively induce ICD to further evoke an anti-cancer immune response.

Besides, as described above, IDO1 is always overexpressed in malignancies and can mediate the catalysis rate-limiting step in converting Trp into Kyn, immunosuppression. Therefore, the expression and cellular activity of IDO1 in 4T1 cells were also measured after treatment with different drug formulations. It is found that all the drug formulations had no significant impact on IDO1 expression in 4T1 cells (Fig. 4H and Fig. S10). As we know, CUR can suppress the IDO1 activity, so the formulation containing CUR may be able to remarkably inhibit the Trp metabolic action. Additionally, due to the suppressible ability of PTX on cellular activity, PTX may also inhibit the Kyn pathway of Trp degradation. Thus, it was observed that the synergism of PTX and CUR enhanced the inhibitor ratio of Kyn production. Especially for the HA-PAAVB NPs/PTX + CUR group, there was even 82% of Kyn

production being inhibited (Fig. 4I), indicating the cellular activity of IDO1 was significantly influenced by different drug formulations. The decrease of Trp and the increase of Kyn might directly suppress the activation and proliferation of effector T cells while promoting the differentiation of Tregs, which could be the primary cause of HA-PAAVB NPs/PTX + CUR to reverse the tumor immunosuppressive and achieve the better therapeutic efficacy.

### 3.7. *In vivo* biodistribution

To evaluate the biodistribution of HA-PAAVB NPs, 4T1 tumor-bearing balb/c mice were injected intravenously with free DiR and HA-PAAVB NPs/DiR, respectively. Their time-dependent bio-distribution was monitored using the IVIS fluorescence imaging system. As shown in Fig. 5A, the fluorescence intensity of DiR in the mice treated with HA-PAAVB NPs/DiR gradually increased during the whole experiment. In contrast, the fluorescent signal in the mice injected with free DiR was weaker over the experiment period, which might be due to the rapid clearance of free DiR in mice. The major organs, such as heart, liver, spleen, lungs, kidneys and tumors, were harvested for ex vivo fluorescence images at 24 h post-injection. It is exhibited that both free DiR and HA-PAAVB NPs/DiR were mainly accumulated in the liver and spleen. However, the fluorescence intensity of tumors in HA-PAAVB NPs/DiR group was 3.84 times higher than that in the free DiR group, indicating that HA modification on the surface of PAAVB NPs could improve their tumor-targeting capacity (Fig. 5B).

### 3.8. *In vivo* therapeutic efficiency

To evaluate the antitumor effects, the mice received i. v. injection of different drug formulations (6.6 mg of CUR and 3 mg of PTX per kg of

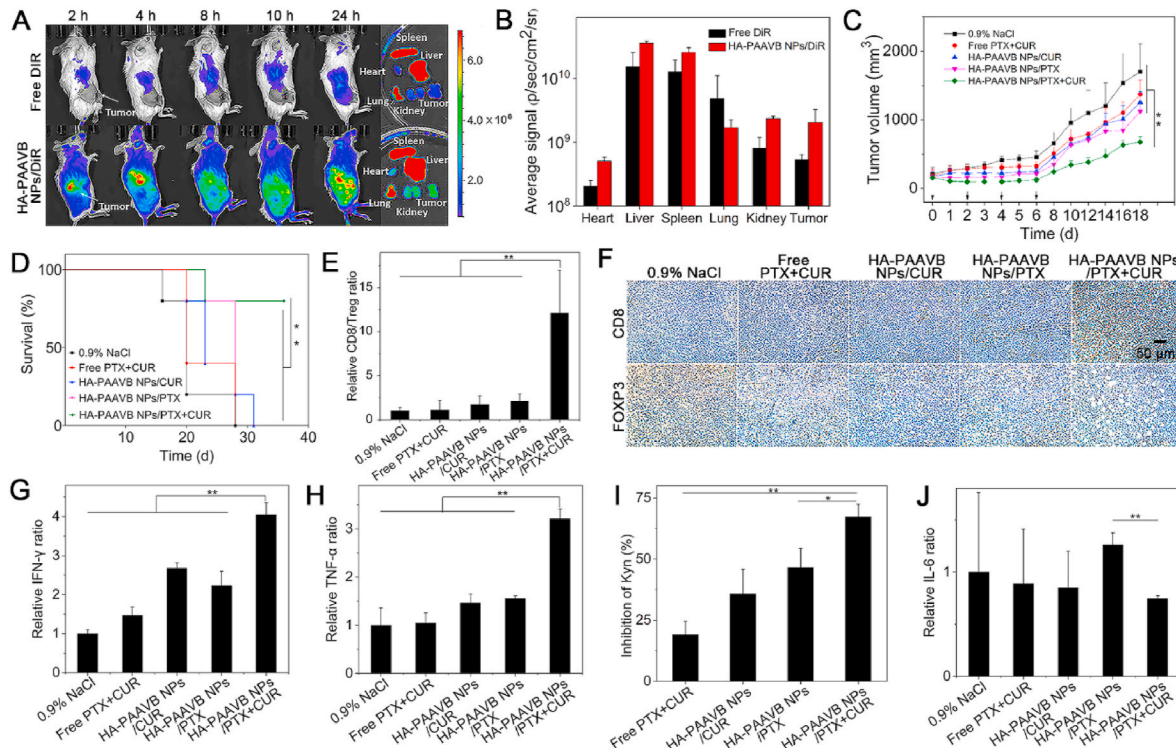


**Fig. 5.** (A) *In vivo* whole animal imaging of 4T1 tumor-bearing mice which were intravenously injected with free DiR and DiR-loaded HA-PAAVB NPs at 2 h, 4 h, 8 h, 10 h and 24 h, and *ex vivo* fluorescence imaging of dissected organs after 24 h post-injection. (B) Quantitative analysis of the fluorescent intensity of DiR in tumor tissue detected by *in vivo* imaging system ( $n = 3$ ). (C) The determination of tumor volume and (D) the survival rates after the mice bearing 4T1 tumors were treated with different drug formulations ( $n = 5$ ). (E) Flow cytometry analysis of CD8<sup>+</sup> CTLs/Tregs ratios in tumor tissue in 4T1 tumor-bearing mice treated with different drug formulations ( $n = 5$ ). (F) IHC staining for CD8 and FOXP3 expression of the tumors from mice at the end of the experiment. Elisa analysis to show the impact of the different drug formulations on (G) IFN- $\gamma$ , (H) TNF- $\alpha$  and (J) IL-6 in plasma at the end of the experiment ( $n = 5$ ).

mice body) four times, when the tumor size grew to  $175 \pm 20.6 \text{ mm}^3$ . As shown in Fig. 5C, although free PTX + CUR, HA-PAAVB NPs/PTX, and HA-PAAVB NPs/CUR suppressed the tumor growth at a relatively low level, the tumor volume in these groups still increased over  $1000 \text{ mm}^3$  at the end of the experiment. However, HA-PAAVB NPs/PTX + CUR achieved enhanced anti-tumor efficiency. For example, the tumor inhibition rate in HA-PAAVB NPs/PTX + CUR group was  $60.3\% \pm 4.4\%$ , which was significantly higher than that of free PTX + CUR ( $19.3\% \pm 12.1\%$ ), HA-PAAVB NPs/CUR ( $26.3\% \pm 9.4\%$ ), and HA-PAAVB NPs/PTX ( $34.1\% \pm 15.6\%$ ) groups. H&E staining image of tumor tissue also

showed that more severe damage induced by HA-PAAVB NPs/PTX + CUR appeared in most areas (Fig. S11). HA-PAAVB NPs/PTX + CUR also significantly prolonged the survival of tumor-bearing mice. Fig. 5D shows that 80% of mice were still alive on day 45, whereas all the mice in other groups died.

To further evaluate whether HA-PAAVB NPs/PTX + CUR could promote the immune activity on attacking tumors, immune phenotyping was performed on the tumors and plasma from the mice in different groups. As shown in Fig. 5E, the CD8<sup>+</sup> T cells/Tregs ratio significantly increased in HA-PAAVB NPs/PTX + CUR group, which was 5.7–12.1

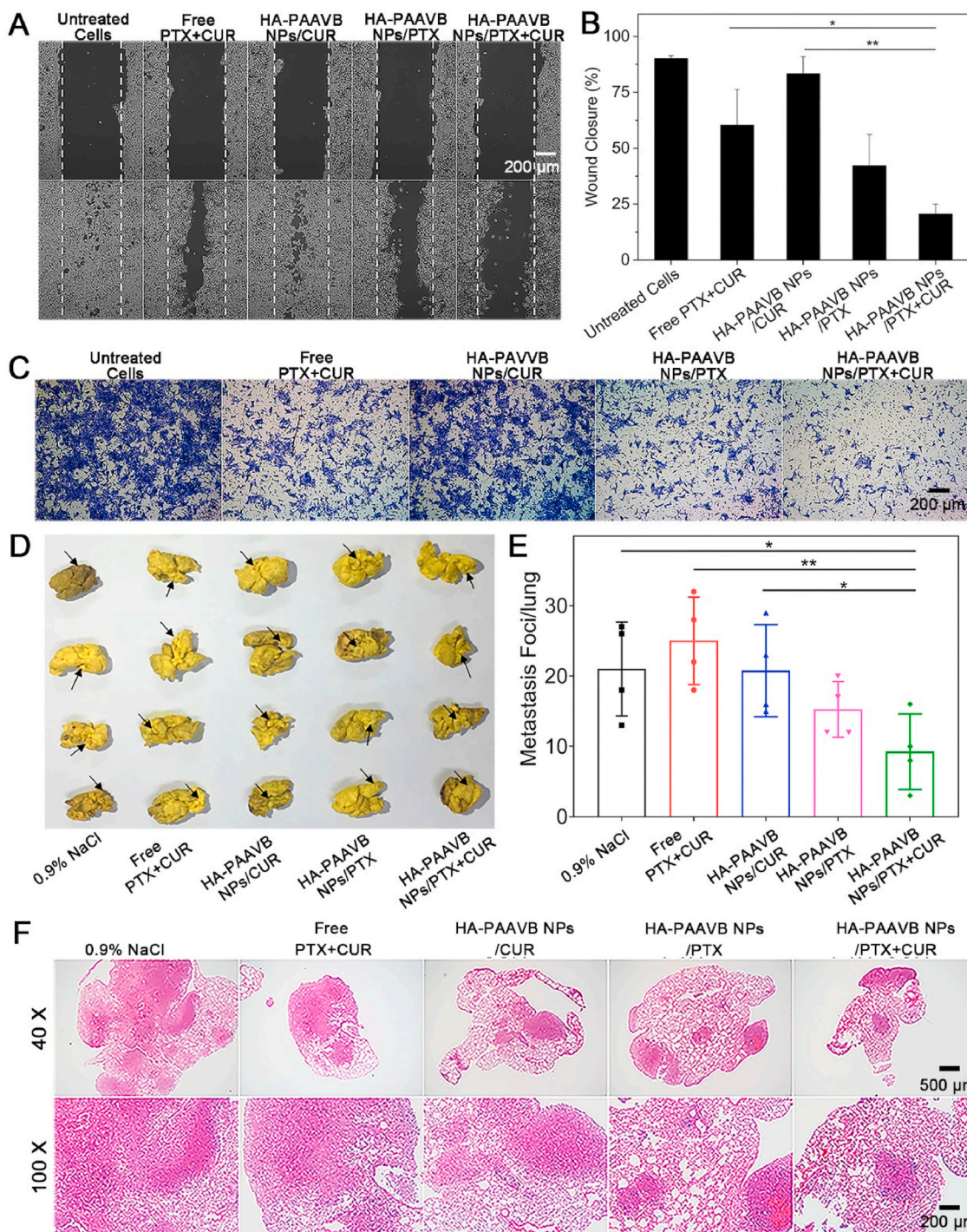


**Fig. 6.** (A) The images and (B) quantitative analysis of wound healing response on 4T1 cells treated with different drug formulations (n = 3). (C) Transwell migration assay on 4T1 cells after being treated with different drug formulations (n = 3). (D) Morphology, (E) Metastasis foci and (F) H&E images of lungs from mice with metastatic breast cancer after the systematic injection of different drug formulations (n = 4). Black arrows represented the foci of tumor metastases (n = 4).

folds higher than other groups. Moreover, the ratio of CD8<sup>+</sup> T and CD4<sup>+</sup> T cells in the HA-PAAVB NPs/PTX + CUR group increased significantly, which was 1.6–2.8 folds and 2.1–4.6 folds higher than other groups, respectively (Fig. S12 A–B). On the contrary, Treg cells in HA-PAAVB NPs/PTX + CUR group significantly decreased 0.76-fold in comparison to 0.9% NaCl group (Fig. S12C). These results were further corroborated by IHC staining for CD8 and Foxp3, where CTLs appeared and Treg disappeared in response to the synergistic effect of PTX and CUR (Fig. 5F). It was also found that the treatment of HA-PAAVB NPs/PTX + CUR boosted the production of IFN- $\gamma$  and TNF- $\alpha$ , which also strengthened effector T cells or attack cancer cells directly (Fig. 5G–H). Meanwhile, HA-PAAVB NPs/PTX + CUR also achieved the strongest suppressible capacity on IDO1 metabolic pathway at the tumor tissue. In Fig. 5I, the treatment of HA-PAAVB NPs/PTX + CUR prevented 67.3%  $\pm$  5.2% of Trp from converting to Kyn. Because the enhanced production of Kyn in the malignant tumor can not only induce effector T-cell arrest but also lead to binding of aryl hydrocarbon receptor (AhR), a ligand-gated transcription factor that is expressed in many immune cells and participate in many immunomodulatory effects [11,22,63–68]. After the Kyn-AhR complexes formation, it will potentiate IL-6 production, which can lead to the aggressive tumor growth [11,65]. Thus, when IDO1 activity was suppressed by the treatment of HA-PAAVB NPs/PTX + CUR, the transcription of IL-6 would be also inhibited, reducing the immunosuppression in the tumor. (Fig. 5J).

Because lung metastasis of breast cancer is responsible for a majority of treatment failures [64,69–71], the efficiency of preventing metastasis was also paid great attention. Therefore, we first assessed the direct impact of drug formulations on the metastatic potential of 4T1 cells *in vitro*. Fig. 6A depicts that the wounds of untreated cells were almost healed after 24 h of incubation, and the single drug formulation only inhibited the wound healing at a limited level. However, free PTX + CUR and HA-PAAVB NPs/PTX + CUR significantly inhibited the wound closure of 4T1 cells in comparison to other groups. The healing rate of HA-PAAVB NPs/PTX + CUR (20.5%) was obviously lower than that of free PTX + CUR (60.4%) (Fig. 6B). Meanwhile, the results of the transwell assay further verified that HA-PAAVB NPs/PTX + CUR possessed the strongest inhibitory effect on 4T1 cell migration compared to other groups (Fig. 6C and Fig. S13). Based on the results above, it is concluded that HA-PAAVB NPs/PTX + CUR could effectively inhibit the migration of 4T1 cells *in vitro*.

In addition, we further examined the effect of drug formulations on the progression of lung metastasis *in vivo*. As depicted in Fig. 6D–E, the average number of lung metastatic nodules in both 0.9% NaCl and free PTX + CUR group exceeded 20. In contrast, drug-loaded HA-PAAVB NPs significantly suppressed breast cancer lung metastasis. Especially for HA-PAAVB NPs/PTX + CUR group, there were less than 9 metastatic nodules appearing in the lung. Meanwhile, the lungs were also harvested for H&E staining after the treatment (Fig. 6F). It is shown that the number of lung metastatic nodules in group HA-PAAVB NPs/PTX + CUR was less than that of other groups, where the area was smaller, further demonstrating that HA-PAAVB NPs/PTX + CUR could be beneficial for the suppression of the lung metastasis of breast cancer.

According to these results, it is demonstrated that this dual drug nanomedicine could induce an immunogenic cell death stimulus to boost immune-response as well as inhibit the regional activity of IDO1 enzyme to prevent Treg proliferation and IL-6 production. Then, the above-mentioned immune-response could reduce the primary tumor growth as well as suppress breast cancer to lung metastases. Thus, we can conclude that the synergistic effect of chemotherapeutic and immunomodulatory therapy of HA-PAAVB NPs/PTX + CUR can enhance therapeutic efficacy both *in vitro* and *in vivo*.

### 3.9. Biosafety

Biosafety is another key issue for the application of nanomedicine in the clinic. Thus, we conducted a series of experiments to evaluate

whether HA-PAAVB NPs/PTX + CUR to be safe *in vivo*. As shown in Fig. S14, the weight of mice treated with HA-PAAVB NPs/PTX + CUR did not change drastically through the whole experiment. In addition, the H&E images showed that HA-PAAVB NPs/PTX + CUR did not have obvious toxicity to the normal tissues (Fig. 7A). Nevertheless, some damages of liver and kidney were observed in the free PTX + CUR group. Additionally, the blood biochemical results also depicted that free PTX + CUR could induce the dysfunction of the liver and kidney. Some major function indexes of the liver (ALT, AST) and kidney (CREA, UREA) in the free PTX + CUR group were remarkably different from those in 0.9% NaCl group (Fig. 7B–E). Meanwhile, the results of blood routine analysis showed that the abnormal content of lymph, MPV, WBC, and Gran appeared in mice treated with free PTX + CUR, indicating that free drug formulation could cause hepatic, renal, and other physical function disorder (Fig. S15).

Furthermore, global hepatic and renal metabolomics analysis was also performed. Based on the metabolomics analytical data of GC/MS, 101 hepatic metabolites, and 95 renal metabolites were identified (Table S3). Through identifying the differential metabolites using the Mann-Whitney-Wilcoxon method, it was found that there were 3 significantly altered renal metabolites in free PTX + CUR group vs. 0.9% NaCl group, such as the increase of L-lysine and decrease of 1-methyl nicotinamide and inosine, while only one significantly altered kidney metabolites (pipecolic acid) were identified in HA-PAAVB NPs/PTX + CUR group (Fig. 7F and Table S4). Since inosine plays an important role in the energy metabolism of the kidney, its downregulation may damage the kidney [72]. Meanwhile, there were 4 significantly altered hepatic metabolites in the free PTX + CUR group vs the 0.9% NaCl group, including the decrease of malonic acid and pyruvic acid and increase of L-lysine and L-Tryptophan, which suggested that there appeared the abnormality in energy metabolism and amino acid metabolism [73]. Additionally, pyruvic acid was an important intermediate in glucose metabolism, connecting glycolysis with the TCA cycle, the decrease of pyruvic acid raised the possibility of abnormal glycolysis in free PTX + CUR group [74]. In contrast, only one significantly altered hepatic metabolites (L-cysteine) in HA-PAAVB NPs/PTX + CUR group vs the 0.9% NaCl group were determined (Fig. 7G and Table S5). These results were also consistent with the finding from the metabolism pathway analysis. In Fig. 7H–I, after the treatment of free PTX + CUR, there was 3 pathways (including biotin metabolism, nicotinate and nicotinamide metabolism, and Lysine degradation) being over-activated through the analysis of renal tissue, whereas only one pathway (Lysine degradation) was activated by the HA-PAAVB NPs/PTX + CUR treatment. Of note in Fig. 7J–K, the pathway analysis of hepatic tissue showed that 2 pathways (Aminoacyl-tRNA biosynthesis and Biotin metabolism) were regulated in the free PTX + CUR group. However, there were 7 pathways being over-activated through the analysis of hepatic tissue in HA-PAAVB NPs/PTX + CUR group, because L-cysteine is a common amino acid in our body and usually participates in multiple metabolic pathways.

Overall, these results show that this targeted and intelligent nanomedicine possesses preferable biosafety for further medical applications. Since that the UCST (>45 °C) of carrier polymer PAAVB was higher than normal physiological temperature, both PTX and CUR were entrapped in the NPs, so the toxic side effects induced by the unspecific drug leakage can be consequently avoided.

## 4. Conclusion

To summarize, a new copolymer PAAVB with controllable UCST that can be tuned by pH and GSH was synthesized and proposed in this paper. Then, a nano-platform was prepared with this copolymer being coated with a HA layer, which demonstrated the capability to specifically deliver PTX and CUR to CD44-overexpressing 4T1 breast cancer. Under the co-existence of an acidic condition and a high level of GSH (lysosome of cancer cells), electrostatic repulsion was enhanced due to imidazole protonation and the molecular weight dropped by cause of disulfide

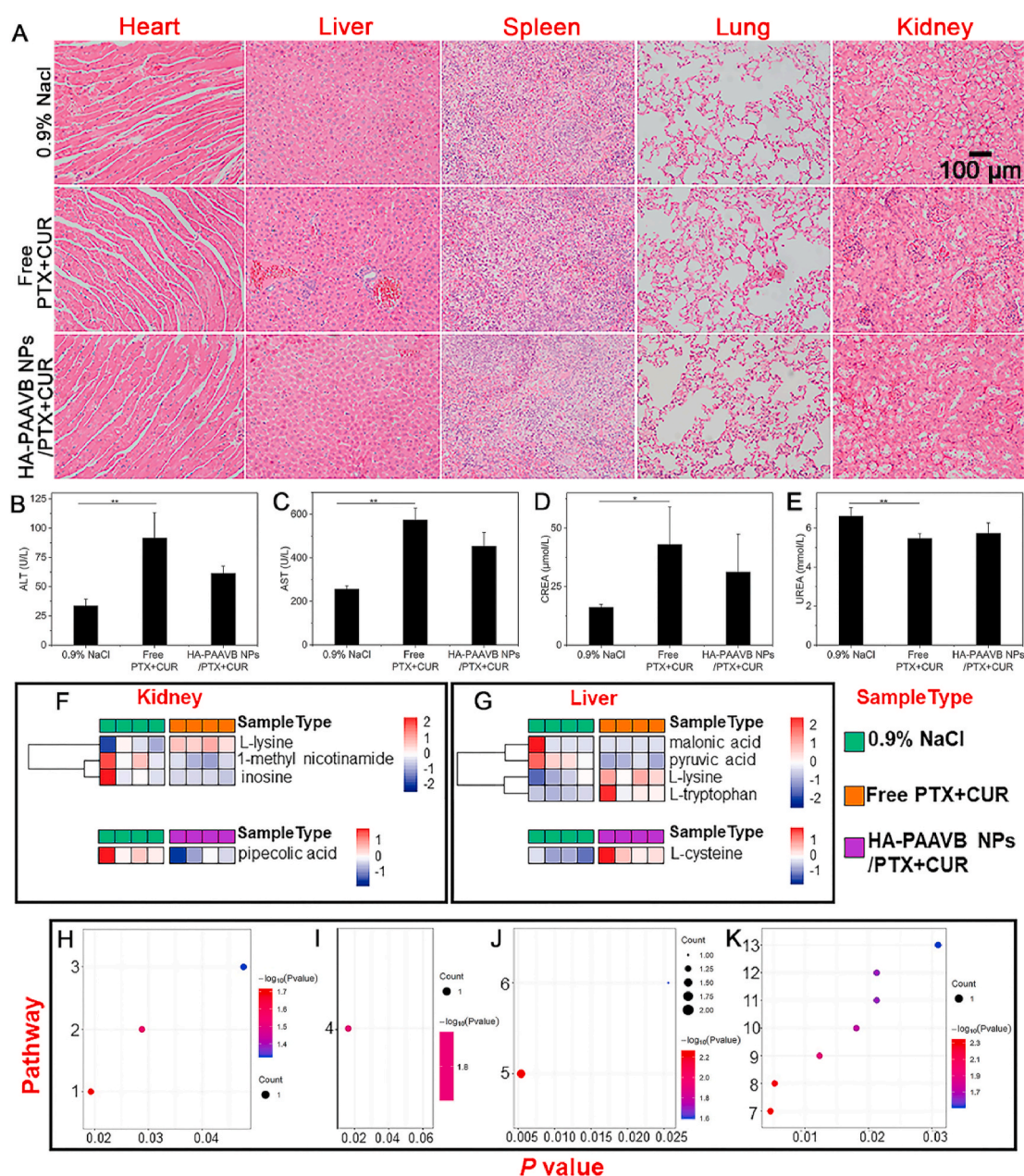


**Fig. 7.** (A) H&E images of the different organs slices from mice on day 18 after the administration of varying drug formulations for three times. (B–E) The changes of serum AST, ALT, CREA and UREA levels on day 18 (n = 4). Heatmap analysis of the metabolites between different drug formulations groups in (F) kidney and (G) liver. Significantly altered metabolic pathways in kidney (H) Free PTX + CUR group vs. 0.9% NaCl group and (I) HA-PAAVB NPs/PTX + CUR group vs. 0.9% NaCl group. Significantly altered metabolic pathways in liver (J) Free PTX + CUR group vs. 0.9% NaCl group and (K) HA-PAAVB NPs/PTX + CUR group vs. 0.9% NaCl group. (1: Biotin metabolism, 2: Nicotinate and nicotinamide metabolism, 3: Lysine degradation, 4: Lysine degradation, 5: Aminoacyl-tRNA biosynthesis, 6: Biotin metabolism, 7: Thiamine metabolism, 8: Taurine and hypotaurine metabolism, 9: Pantothenate and CoA biosynthesis, 10: Glutathione metabolism, 11: Glycine, serine and threonine metabolism, 12: Cysteine and methionine metabolism, 13: Aminoacyl-tRNA biosynthesis). Heatmap's color is determined by the relative expression, the red represents upregulated, blue represents downregulated. The size of the pathway's circle is determined by the number of metabolic metabolites, and its color is determined by the P value (n = 4). (For interpretation of the references to color in this figure legend, the reader is referred to the Web version of this article.)

reduction. Consequently, hydrogen bonds among the polymers were directly weakened or even overruled, which led to the decrease of the polymer's UCST and the disassembly of HA-PAAVB NPs. This distinctive behavior precisely controlled the drug release to avoid the unspecific drug leakage and their toxic side effects, which also significantly improved the capacity of PTX on inducing immunogenic death of cancer cells and CUR on reversing the IDO1 enzyme-mediated tumor immunosuppression. In addition, the enhanced synergistic effect of PTX and CUR that was mediated by HA-PAAVB NPs could inhibit primary breast

cancer growth and their lung metastasis. Therefore, the intelligent drug delivery system [75–84] based PAAVB copolymer presented in this paper could provide an effective platform that combines chemo- and immune-therapeutics for fighting against various malignant tumors.

#### Declaration of competing interest

All authors declared no competing interests.

## CRedit authorship contribution statement

**Ying Wang:** Investigation, Methodology, Data curation, Formal analysis, Writing - original draft. **Di Gao:** Investigation, Methodology, Data curation, Formal analysis, Writing - original draft. **Yan Liu:** Investigation, Discussion, Writing - review & editing. **Xiaoqing Guo:** Investigation, Methodology. **Shuojia Chen:** Investigation. **Li Zeng:** Resources. **Jinxuan Ma:** Investigation. **Xingcai Zhang:** Supervision, Conceptualization, Methodology, Writing - review & editing. **Zhongmin Tian:** Funding acquisition, Conceptualization, Supervision, Writing - review & editing, Project administration. **Zhe Yang:** Conceptualization, Methodology, Formal analysis, Data curation, Writing - review & editing, Supervision, Funding acquisition.

## Declaration of competing interest

There are no conflicts to declare.

## Acknowledgements

This research was supported by the National Natural Science Foundation of China (51703178, 51903203, 81770728), the China Postdoctoral Science Foundation (2019M663742, 2019M653661), Natural Science Foundation of Zhejiang Province (LWY20H180002).

## Appendix B. Supplementary data

Supplementary data related to this article can be found at <https://doi.org/10.1016/j.bioactmat.2020.11.016>.

## References

- [1] L. Huang, Y. Li, Y. Du, Y. Zhang, X. Wang, Y. Ding, X. Yang, F. Meng, J. Tu, L. Luo, C. Sun, Mild photothermal therapy potentiates anti-PD-L1 treatment for immunologically cold tumors via an all-in-one and all-in-control strategy, *Nat. Commun.* 10 (1) (2019) 4871, <https://doi.org/10.1038/s41467-019-12771-9>.
- [2] L.L. Dai, K. Li, M.H. Li, X.J. Zhao, Z. Luo, L. Lu, Y.F. Luo, K.Y. Cai, Size/charge changeable acidity-responsive micelleplex for photodynamic-improved PD-L1 immunotherapy with enhanced tumor penetration, *Adv. Funct. Mater.* 28 (18) (2018) 1707249, <https://doi.org/10.1002/adfm.201707249>.
- [3] G.C. Prendergast, A. Mondal, S. Dey, L.D. Laury-Kleintop, A.J. Muller, Inflammatory reprogramming with Ido1 inhibitors: turning immunologically unresponsive 'cold' tumors 'hot', *Trends Cancer* 4 (1) (2018) 38–58, <https://doi.org/10.1016/j.trecan.2017.11.005>.
- [4] A.C. Huang, M.A. Postow, R.J. Orlowski, R. Mick, B. Bengsch, S. Manne, W. Xu, S. Harmon, J.R. Giles, B. Wenz, M. Adamow, D. Kuk, K.S. Panageas, C. Carrera, P. Wong, F. Quagliarello, B. Wubbenhorst, K. D'Andrea, K.E. Pauken, R.S. Herati, R.P. Staup, J.M. Schenkel, S. McGettigan, S. Kothari, S.M. George, R. H. Vonderheide, R.K. Amaravadi, G.C. Karakousis, L.M. Schuchter, X. Xu, K. L. Nathanson, J.D. Wolchok, T.C. Gangadhar, E.J. Wherry, T-cell invigoration to tumour burden ratio associated with anti-PD-1 response, *Nature* 545 (7652) (2017) 60–65, <https://doi.org/10.1038/nature22079>.
- [5] B. Feng, F.Y. Zhou, B. Hou, D.G. Wang, T.T. Wang, Y.L. Fu, Y.T. Ma, H.J. Yu, Y. P. Li, Binary cooperative prodrug nanoparticles improve immunotherapy by synergistically modulating immune tumor microenvironment, *Adv. Mater.* 30 (38) (2018) 1803001, <https://doi.org/10.1002/adma.201803001>.
- [6] X.D. Liu, N. Shin, H.K. Koblisch, G.J. Yang, Q. Wang, K. Wang, L. Leffet, M. J. Hansbury, B. Thomas, M. Rupa, P. Waeltz, K.J. Bowman, P. Polam, R.B. Sparks, E.W. Yue, Y.L. Li, R. Wynn, J.S. Fridman, T.C. Burn, A.P. Combs, R.C. Newton, P. A. Scherle, Selective inhibition of Ido1 effectively regulates mediators of antitumor immunity, *Blood* 115 (17) (2010) 3520–3530, <https://doi.org/10.1182/blood-2009-09-246124>.
- [7] A.L. Mellor, D.H. Munn, Ido expression by dendritic cells: tolerance and tryptophan catabolism, *Nat. Rev. Immunol.* 4 (10) (2004) 762–774, <https://doi.org/10.1038/nri1457>.
- [8] Y. Chen, R. Xia, Y. Huang, W. Zhao, J. Li, X. Zhang, P. Wang, R. Venkataramanan, J. Fan, W. Xie, X. Ma, B. Lu, S. Li, An immunostimulatory dual-functional nanocarrier that improves cancer immunotherapy, *Nat. Commun.* 7 (2016) 13443, <https://doi.org/10.1038/ncomms13443>.
- [9] S. Ninomiya, N. Narala, L. Huye, S. Yagyu, B. Savoldo, G. Dotti, H.E. Heslop, M. K. Brenner, C.M. Rooney, C.A. Ramos, Tumor indoleamine 2,3-dioxygenase (Ido) inhibits CD19-CAR T cells and is downregulated by lymphodepleting drugs, *Blood* 125 (25) (2015) 3905–3916, <https://doi.org/10.1182/blood-2015-01-621474>.
- [10] R. Potula, L. Poluektova, B. Knipe, J. Chrastil, D. Heilman, H.Y. Dou, O. Takikawa, D.H. Munn, H.E. Gendelman, Y. Persidsky, Inhibition of indoleamine 2,3-dioxygenase (Ido) enhances elimination of virus-infected macrophages in an animal model of HIV-1 encephalitis, *Blood* 106 (7) (2005) 2382–2390, <https://doi.org/10.1182/blood-2005-04-1403>.
- [11] C. Uyttenhove, L. Pilotte, I. Théate, V. Stroobant, D. Colau, N. Parmentier, T. Boon, B.J. Van den Eynde, Evidence for a tumoral immune resistance mechanism based on tryptophan degradation by indoleamine 2,3-dioxygenase, *Nat. Med.* 9 (10) (2003) 1269–1274, <https://doi.org/10.1038/nm934>.
- [12] R.B. Holmgaard, D. Zamarin, Y.Y. Li, B. Gasmi, D.H. Munn, J.P. Allison, T. Merghoub, J.D. Wolchok, Tumor-expressed Ido recruits and activates MDSCs in a Treg-dependent manner, *Cell Rep.* 13 (2) (2015) 412–424, <https://doi.org/10.1016/j.celrep.2015.08.077>.
- [13] S.J. Yu, C. Wang, J.C. Yu, J.Q. Wang, Y. Lu, Y.Q. Zhang, X.D. Zhang, Q.Y. Hu, W. J. Sun, C.L. He, X.S. Chen, Z. Gu, Injectable bioresponsive gel depot for enhanced immune checkpoint blockade, *Adv. Mater.* 30 (28) (2018) 1801527, <https://doi.org/10.1002/adma.201801527>.
- [14] G.C. Prendergast, W.P. Malachowski, J.B. DuHadaway, A.J. Muller, Discovery of Ido1 inhibitors: from bench to bedside, *Canc. Res.* 77 (24) (2017) 6795–6811, <https://doi.org/10.1158/0008-5472.CAN-17-2285>.
- [15] H.K. Koblisch, M.J. Hansbury, K.J. Bowman, G.J. Yang, C.L. Neilan, P.J. Haley, T. C. Burn, P. Waeltz, R.B. Sparks, E.W. Yue, A.P. Combs, P.A. Scherle, J. V. Fridman, Hydroxyamidine inhibitors of indoleamine-2,3-dioxygenase potentially suppress systemic tryptophan catabolism and the growth of Ido-expressing tumors, *Mol. Canc. Therapeut.* 9 (2) (2010) 489–498, <https://doi.org/10.1158/1535-7163.Mct-09-0628>.
- [16] R. Metz, S. Rust, J.B. DuHadaway, M.R. Mautino, D.H. Munn, N.N. Vahanian, C. J. Link, G.C. Prendergast, Ido inhibits a tryptophan sufficiency signal that stimulates mTOR: a novel Ido effector pathway targeted by D-1-methyl-tryptophan, *Oncolmunology* 1 (9) (2012) 1460–1468, <https://doi.org/10.4161/onci.21716>.
- [17] O. Naksuriya, S. Okonogi, R.M. Schifferlers, W.E. Hennink, Curcumin nanoformulations: a review of pharmaceutical properties and preclinical studies and clinical data related to cancer treatment, *Biomaterials* 35 (10) (2014) 3365–3383, <https://doi.org/10.1016/j.biomaterials.2013.12.090>.
- [18] L. Ray, M.K. Pal, R.S. Ray, Synergism of co-delivered nanosized antioxidants displayed enhanced anticancer efficacy in human colon cancer cell lines, *Bioact. Mater.* 2 (2) (2017) 82–95, <https://doi.org/10.1016/j.bioactmat.2017.02.003>.
- [19] Y.I. Jeong, S.W. Kim, I.D. Jung, J.S. Lee, J.H. Chang, C.M. Lee, S.H. Chun, M. S. Yoon, G.T. Kim, S.W. Ryu, J.S. Kim, Y.K. Shin, W.S. Lee, H.K. Shin, J.D. Lee, Y. M. Park, Curcumin suppresses the induction of indoleamine 2,3-dioxygenase by blocking the Janus-activated kinase-protein kinase Cdelta-STAT1 signaling pathway in interferon-gamma-stimulated murine dendritic cells, *J. Biol. Chem.* 284 (6) (2009) 3700–3708, <https://doi.org/10.1074/jbc.M807328200>.
- [20] I.D. Jung, Y.I. Jeong, C.M. Lee, K.T. Noh, S.K. Jeong, S.H. Chun, O.H. Choi, W. S. Park, J. Han, Y.K. Shin, H.W. Kim, C.H. Yun, Y.M. Park, COX-2 and PGE2 signaling is essential for the regulation of Ido expression by curcumin in murine bone marrow-derived dendritic cells, *Int. Immunopharm.* 10 (7) (2010) 760–768, <https://doi.org/10.1016/j.intimp.2010.04.006>.
- [21] H. Huang, C.-T. Jiang, S. Shen, A. Liu, Y.-J. Gan, Q.-S. Tong, S.-B. Chen, Z.-X. Gao, J.-Z. Du, J. Cao, J. Wang, Nanoenabled reversal of Ido1-mediated immunosuppression synergizes with immunogenic chemotherapy for improved cancer therapy, *Nano Lett.* 19 (8) (2019) 5356–5365, <https://doi.org/10.1021/acs.nanolett.9b01807>.
- [22] J. Lu, X. Liu, Y.-P. Liao, F. Salazar, B. Sun, W. Jiang, C.H. Chang, J. Jiang, X. Wang, A.M. Wu, H. Meng, A.E. Nel, Nano-enabled pancreas cancer immunotherapy using immunogenic cell death and reversing immunosuppression, *Nat. Commun.* 8 (1) (2017) 1811, <https://doi.org/10.1038/s41467-017-01651-9>.
- [23] L. Zitvogel, O. Kepp, L. Senovilla, L. Menger, N. Chaput, G. Kroemer, Immunogenic tumor cell death for optimal anticancer therapy: the calcitriol exposure pathway, *Clin. Canc. Res.* 16 (12) (2010) 3100–3104, <https://doi.org/10.1158/1078-0432.CCR-09-2891>.
- [24] I. Martins, Y. Wang, M. Michaud, Y. Ma, A.Q. Sukkurwala, S. Shen, O. Kepp, D. Métivier, L. Galluzzi, J.L. Perfettini, L. Zitvogel, G. Kroemer, Molecular mechanisms of ATP secretion during immunogenic cell death, *Cell Death Differ.* 21 (1) (2014) 79–91, <https://doi.org/10.1038/cdd.2013.75>.
- [25] B. Feng, B. Hou, Z.A. Xu, M. Saeed, H.J. Yu, Y.P. Li, Self-amplified drug delivery with light-inducible nanocargoes to enhance cancer immunotherapy, *Adv. Mater.* 31 (40) (2019) 1902960, <https://doi.org/10.1002/adma.201902960>.
- [26] J. Zhou, Y. Liu, G. Zhang, Q. Jia, L. Li, DNA-templated porous nanoplatform towards programmed "double-hit" cancer therapy via hyperthermia and immunogenicity activation, *Biomaterials* 219 (2019) 119395, <https://doi.org/10.1016/j.biomaterials.2019.119395>.
- [27] W. Yu, X. He, Z. Yang, X. Yang, W. Xiao, R. Liu, R. Xie, L. Qin, H. Gao, Sequentially responsive biomimetic nanoparticles with optimal size in combination with checkpoint blockade for cascade synergetic treatment of breast cancer and lung metastasis, *Biomaterials* 217 (2019) 119309, <https://doi.org/10.1016/j.biomaterials.2019.119309>.
- [28] X. Liu, D. Wang, P. Zhang, Y. Li, Recent advances in nanosized drug delivery systems for overcoming the barriers to anti-PD immunotherapy of cancer, *Nano Today* 29 (2019) 100801, <https://doi.org/10.1016/j.nantod.2019.100801>.
- [29] K. Sasaki, J. Ishihara, A. Ishihara, R. Miura, A. Mansurov, K. Fukunaga, J. A. Hubbell, Engineered collagen-binding serum albumin as a drug conjugate carrier for cancer therapy, *Sci. Adv.* 5 (8) (2019), eaaw6081, <https://doi.org/10.1126/sciadv.aaw6081>.
- [30] G. Kroemer, L. Galluzzi, O. Kepp, L. Zitvogel, Immunogenic cell death in cancer therapy, *Annu. Rev. Immunol.* 31 (2013) 51–72, <https://doi.org/10.1146/annurev-immunol-032712-100008>.

- [31] H.H. Soliman, E. Jackson, T. Neuger, E.C. Dees, R.D. Harvey, H. Han, R. Ismail-Khan, S. Minton, N.N. Vahanian, C. Link, D.M. Sullivan, S. Antonia, A first in man phase I trial of the oral immunomodulator, indoximod, combined with docetaxel in patients with metastatic solid tumors, *Oncotarget* 5 (18) (2014) 8136–8146, <https://doi.org/10.18632/oncotarget.2357>.
- [32] P. Pattekar, Z. Zheng, X. Zhang, T. Levchenko, V. Torchilin, Y. Lvov, Top-down and bottom-up approaches in production of aqueous nanocolloids of low solubility drug paclitaxel, *Phys. Chem. Chem. Phys.* 13 (19) (2011) 9014–9019, <https://doi.org/10.1039/c0cp02549f>.
- [33] Z. Yang, N. Kong, X. Zhang, Y. Liu, P. Hu, S. Mou, P. Liljestrom, J. Shi, W. Tan, J. S. Kim, Y. Cao, R. Langer, K.W. Leong, O.C. Farokhzad, W. Tao, A materials-science perspective on tackling COVID-19, *Nat. Rev. Mater.* 5 (2020) 847–860, <https://doi.org/10.1038/s41578-020-00247-y>.
- [34] V. Vergara, F. Scarlino, C. Bellomo, R. Rinaldi, D. Vergara, M. Maffia, F. Baldassarre, G. Giannelli, X. Zhang, Y. Lvov, S. Leporatti, Drug-loaded polyelectrolyte microcapsules for sustained targeting of cancer cells, *Adv. Drug Deliv. Rev.* 63 (9) (2011) 847–863, <https://doi.org/10.1016/j.addr.2011.05.007>.
- [35] D. Gao, X. Guo, X. Zhang, S. Chen, Y. Wang, T. Chen, G. Huang, Y. Gao, Z. Tian, Z. Yang, Multifunctional phototheranostic nanomedicine for cancer imaging and treatment, *Materials Today Bio* 5 (2019) 100035, <https://doi.org/10.1016/j.mtbio.2019.100035>.
- [36] G. Parekh, Y. Shi, J. Zheng, X. Zhang, S. Leporatti, Nano-carriers for targeted delivery and biomedical imaging enhancement, *Ther. Deliv.* 9 (2018) 451–468, <https://doi.org/10.4155/tde-2018-0013>.
- [37] Z. Yang, R. Cheng, C. Zhao, N. Sun, H. Luo, Y. Chen, Z. Liu, X. Li, J. Liu, Z. Tian, Thermo- and pH-dual responsive polymeric micelles with upper critical solution temperature behavior for photoacoustic imaging-guided synergistic chemophotothermal therapy against subcutaneous and metastatic breast tumors, *Theranostics* 8 (15) (2018) 4097–4115, <https://doi.org/10.7150/thno.26195>.
- [38] J. Niskanen, H. Tenhu, How to manipulate the upper critical solution temperature (UCST)? *Polym. Chem.* 8 (1) (2017) 220–232, <https://doi.org/10.1039/c6py01612j>.
- [39] J. Seuring, S. Agarwal, First example of a universal and cost-effective approach: polymers with tunable upper critical solution temperature in water and electrolyte solution, *Macromolecules* 45 (9) (2012) 3910–3918, <https://doi.org/10.1021/ma300355k>.
- [40] F.A. Plamper, A. Schmalz, M. Ballauff, A.H.E. Muller, Tuning the thermo-responsiveness of weak polyelectrolytes by pH and light: lower and upper critical-solution temperature of Poly(N,N-dimethylaminoethyl methacrylate), *J. Am. Chem. Soc.* 129 (47) (2007) 14538–14539, <https://doi.org/10.1021/ja074720i>.
- [41] J. Niskanen, C. Wu, M. Ostrowski, G.G. Fuller, S. Hietala, H. Tenhu, Thermo-responsiveness of PDMAEMA. electrostatic and stereochemical effects, *Macromolecules* 46 (6) (2013) 2331–2340, <https://doi.org/10.1021/ma302648w>.
- [42] E. Karjalainen, V. Aseyev, H. Tenhu, Influence of hydrophobic anion on solution properties of PDMAEMA, *Macromolecules* 47 (6) (2014) 2103–2111, <https://doi.org/10.1021/ma5000706>.
- [43] O. Bertrand, A. Vlad, R. Hoogenboom, J.-F. Gohy, Redox-controlled upper critical solution temperature behaviour of a nitroxide containing polymer in alcohol–water mixtures, *Polym. Chem.* 7 (5) (2016) 1088–1095, <https://doi.org/10.1039/c5py01864a>.
- [44] X. Jia, D. Chen, M. Jiang, Preparation of PEO-b-P2VPH+-S2O8(2-) micelles in water and their reversible UCST and redox-responsive behavior, *ChemComm* 16 (2006) 1736–1738, <https://doi.org/10.1039/b600859c>.
- [45] Z. Yang, N. Sun, R. Cheng, C. Zhao, J. Liu, Z. Tian, Hybrid nanoparticles coated with hyaluronic acid lipid for targeted co-delivery of paclitaxel and curcumin to synergistically eliminate breast cancer stem cells, *J. Mater. Chem. B* 5 (33) (2017) 6762–6775, <https://doi.org/10.1039/c7tb01510k>.
- [46] Y. Lv, C. Xu, X. Zhao, C. Lin, X. Yang, X. Xin, L. Zhang, C. Qin, X. Han, L. Yang, W. He, L. Yin, Nanoplatfrom assembled from a CD44-targeted prodrug and smart liposomes for dual targeting of tumor microenvironment and cancer cells, *ACS Nano* 12 (2) (2018) 1519–1536, <https://doi.org/10.1021/acs.nano.7b08051>.
- [47] Q. Hu, X. Gao, T. Kang, X. Feng, D. Jiang, Y. Tu, Q. Song, L. Yao, X. Jiang, H. Chen, J. Chen, CGKRK-modified nanoparticles for dual-targeting drug delivery to tumor cells and angiogenic blood vessels, *Biomaterials* 34 (37) (2013) 9496–9508, <https://doi.org/10.1016/j.biomaterials.2013.09.001>.
- [48] Z. Yang, Y.Q. Li, J.B. Gao, Z. Cao, Q. Jiang, J. Liu, pH and redox dual-responsive multifunctional gene delivery with enhanced capability of transporting DNA into the nucleus, *Colloids Surf. B. Colloids and Surfaces B: Biointerfaces* 153 (2017) 111–122, <https://doi.org/10.1016/j.colsurfb.2017.02.016>.
- [49] G. Huang, H. Li, S.-T. Feng, X. Li, G. Tong, J. Liu, C. Quan, Q. Jiang, C. Zhang, Z. Li, Self-assembled UCST-type micelles as potential drug carriers for cancer therapeutics, *Macromol. Chem. Phys.* 216 (9) (2015) 1014–1023, <https://doi.org/10.1002/macp.201400546>.
- [50] S.L. Levit, H. Yang, C. Tang, Rapid self-assembly of polymer nanoparticles for synergistic codelivery of paclitaxel and lapatinib via flash nano precipitation, *Nanomaterials* 10 (3) (2020) 561, <https://doi.org/10.3390/nano10030561>.
- [51] G. Yu, Z. Yang, X. Fu, B.C. Yung, J. Yang, Z. Mao, L. Shao, B. Hua, Y. Liu, F. Zhang, Q. Fan, S. Wang, O. Jacobson, A. Jin, C. Gao, X. Tang, F. Huang, X. Chen, Polyrotaxane-based supramolecular theranostics, *Nat. Commun.* 9 (1) (2018), <https://doi.org/10.1038/s41467-018-03119-w>, 766–766.
- [52] Y. Ye, J. Wang, Q. Hu, G.M. Hochu, H. Xin, C. Wang, Z. Gu, Synergistic transcutaneous immunotherapy enhances antitumor immune responses through delivery of checkpoint inhibitors, *ACS Nano* 10 (9) (2016) 8956–8963, <https://doi.org/10.1021/acs.nano.6b04989>.
- [53] Z. Yang, N. Sun, R. Cheng, C. Zhao, Z. Liu, X. Li, J. Liu, Z. Tian, pH multistage responsive micellar system with charge-switch and PEG layer detachment for co-delivery of paclitaxel and curcumin to synergistically eliminate breast cancer stem cells, *Biomaterials* 147 (2017) 53–67, <https://doi.org/10.1016/j.biomaterials.2017.09.013>.
- [54] Q. Lv, C.L. He, F.L. Quan, S.J. Yu, X.S. Chen, DOX/IL-2/IFN-gamma co-loaded thermo-sensitive polypeptide hydrogel for efficient melanoma treatment, *Bioact. Mater.* 3 (1) (2018) 118–128, <https://doi.org/10.1016/j.bioactmat.2017.08.003>.
- [55] F. Wilcoxon, Individual comparisons by ranking methods, *Biometrics Bull.* 1 (6) (1945) 80–83, <https://doi.org/10.2307/3001968>.
- [56] H.B. Mann, D.R. Whitney, On a test of whether one of 2 random variables is stochastically larger than the other, *Ann. Math. Stat.* 18 (1) (1947) 50–60, <https://doi.org/10.1214/aoms/1177730491>.
- [57] H.A. David, J.L. Gunnink, The paired t test under artificial pairing, *Am. Statistician* 51 (1) (1997) 9–12, <https://doi.org/10.2307/2684684>.
- [58] K. Li, D. Li, L. Zhao, Y.H. Chang, Y. Zhang, Y. Cui, Z. Y. Zhang, Calcium-mineralized polypeptide nanoparticle for intracellular drug delivery in osteosarcoma chemotherapy, *Bioact. Mater.* 5 (3) (2020) 721–731, <https://doi.org/10.1016/j.bioactmat.2020.04.010>.
- [59] Z. Yang, H.Y. Luo, Z. Cao, Y. Chen, J.B. Gao, Y.Q. Li, Q. Jiang, R.H. Xu, J. Liu, Dual-targeting hybrid nanoparticles for the delivery of SN38 to Her 2 and CD44 overexpressed human gastric cancer, *Nanoscale* 8 (22) (2016) 11543–11558, <https://doi.org/10.1039/c6nr01749e>.
- [60] D. Gao, R.C.H. Wong, Y. Wang, X. Guo, Z. Yang, P.-C. Lo, Shifting the absorption to the near-infrared region and inducing a strong photothermal effect by encapsulating zinc(II) phthalocyanine in poly(lactic-co-glycolic acid)-hyaluronic acid nanoparticles, *Acta Biomater.* 116 (2020) 329–343, <https://doi.org/10.1016/j.actbio.2020.08.042>.
- [61] H. Wang, P. Agarwal, S. Zhao, R.X. Xu, J. Yu, X. Lu, X. He, Hyaluronic acid-decorated dual responsive nanoparticles of Pluronic F127, PLGA, and chitosan for targeted co-delivery of doxorubicin and irinotecan to eliminate cancer stem-like cells, *Biomaterials* 72 (2015) 74–89, <https://doi.org/10.1016/j.biomaterials.2015.08.048>.
- [62] F. Chen, Y. Zhao, Y. Pan, X. Xue, X. Zhang, A. Kumar, X.-J. Liang, Synergistically enhanced therapeutic effect of a carrier-free HCPT/DOX nanodrug on breast cancer cells through improved cellular drug accumulation, *Mol. Pharm.* 12 (7) (2015) 2237–2244, <https://doi.org/10.1021/mp500774m>.
- [63] U.M. Litzenburger, C.A. Opitz, F. Sahn, K.J. Rauschenbach, S. Trump, M. Winter, M. Ott, K. Ochs, C. Lutz, X.D. Liu, N. Anastasov, I. Lehmann, T. Hofer, A. von Deimling, W. Wick, M. Platten, Constitutive Ido expression in human cancer is sustained by an autocrine signaling loop involving IL-6, STAT3 and the AHR, *Oncotarget* 5 (4) (2014) 1038–1051, <https://doi.org/10.18632/oncotarget.1637>.
- [64] J. Lu, X. Liu, Y.-P. Liao, X. Wang, A. Ahmed, W. Jiang, Y. Ji, H. Meng, A.E. Nel, Breast cancer chemo-immunotherapy through liposomal delivery of an immunogenic cell death stimulus plus interference in the Ido-1 pathway, *ACS Nano* 12 (11) (2018) 11041–11061, <https://doi.org/10.1021/acs.nano.8b05189>.
- [65] F.X. Li, L.J. Wei, S.X. Li, J.T. Liu, Indoleamine-2,3-dioxygenase and interleukin-6 associated with tumor response to neoadjuvant chemotherapy in breast cancer, *Oncotarget* 8 (64) (2017) 107844–107858, <https://doi.org/10.18632/oncotarget.22253>.
- [66] B.W. Labadie, R.Y. Bao, J.J. Luke, Reimagining Ido pathway inhibition in cancer immunotherapy via downstream focus on the tryptophan-kynurenine-aryl hydrocarbon axis, *Clin. Canc. Res.* 25 (5) (2019) 1462–1471, <https://doi.org/10.1158/1078-0432.Ccr-18-2882>.
- [67] A.A.-B. Badawy, Kynurenine pathway of tryptophan metabolism: regulatory and functional aspects, *Int. J. Tryptophan Res.* 10 (2017), 1178646917691938.
- [68] E. Wirthgen, A. Hoeflich, Endotoxin-induced tryptophan degradation along the kynurenine pathway: the role of indoleamine 2,3-Dioxygenase and aryl hydrocarbon receptor-mediated immunosuppressive effects in endotoxin tolerance and cancer and its implications for immunoparalysis, *J. Amino Acids* (2015) 973548, <https://doi.org/10.1155/2015/973548>.
- [69] X. He, X. Bao, H. Cao, Z. Zhang, Q. Yin, W. Gu, L. Chen, H. Yu, Y. Li, Tumor-penetrating nanotherapeutics loading a near-infrared probe inhibit growth and metastasis of breast cancer, *Adv. Funct. Mater.* 25 (19) (2015) 2831–2839, <https://doi.org/10.1002/adfm.201500772>.
- [70] W. Xiao, S. Zheng, A. Yang, X. Zhang, P. Liu, X. Xie, H. Tang, X. Xie, Incidence and survival outcomes of breast cancer with synchronous hepatic metastases: a population-based study, *J. Canc.* 9 (23) (2018) 4306–4313, <https://doi.org/10.7150/jca.29190>.
- [71] W. Xiao, S. Zheng, A. Yang, X. Zhang, Y. Zou, H. Tang, X. Xie, Breast cancer subtypes and the risk of distant metastasis at initial diagnosis: a population-based study, *Canc. Manag. Res.* 10 (2018) 5329, <https://doi.org/10.2147/CMAR.S176763>.
- [72] C. Doyle, V. Cristofaro, M.P. Sullivan, R.M. Adam, Inosine – a multifunctional treatment for complications of neurologic injury, *Cell. Physiol. Biochem.* 49 (6) (2018) 2293–2303, <https://doi.org/10.1159/000493831>.
- [73] N. Sun, C. Zhao, R. Cheng, Z. Liu, X. Li, A. Lu, Z. Tian, Z. Yang, Cargo-free nanomedicine with pH sensitivity for codelivery of DOX conjugated prodrug with SN38 to synergistically eradicate breast cancer stem cells, *Mol. Pharm.* 15 (8) (2018) 3343–3355, <https://doi.org/10.1021/acs.molpharmaceut.8b00367>.
- [74] L. Wang, E. Hou, Z. Wang, N. Sun, L. He, L. Chen, M. Liang, Z. Tian, Analysis of metabolites in plasma reveals distinct metabolic features between dahl salt-sensitive rats and consomic SS.13BN rats, *Biochemi Bioph Res Co* 450 (1) (2014) 863–869, <https://doi.org/10.1016/j.bbrc.2014.06.089>.
- [75] X. Zhang, G. Parekh, B. Guo, X. Huang, Y. Dong, W. Han, X. Chen, G. Xiao, Polyphenol and self-assembly: metal polyphenol nanonetwork for drug delivery

- and pharmaceutical applications, *Future Drug Discov* 1 (1) (2019) FDD7, <https://doi.org/10.4155/fdd-2019-0001>.
- [76] D. Vergara, C. Bellomo, X. Zhang, V. Vergaro, A. Tinelli, V. Lorusso, R. Rinaldi, Y. Lvov, S. Leporatti, M. Maffia, Lapatinib/Paclitaxel polyelectrolyte nanocapsules for overcoming multidrug resistance in ovarian cancer, *Nanomedicine:NBM* 8 (6) (2012) 891–899, <https://doi.org/10.1016/j.nano.2011.10.014>.
- [77] M. Zhou, X. Zhang, J. Xie, R. Qi, H. Lu, S. Leporatti, J. Chen, Y. Hu, pH-sensitive poly ( $\beta$ -amino ester)s nanocarriers facilitate the inhibition of drug resistance in breast cancer cells, *Nanomaterials* 8 (11) (2018) 952, <https://doi.org/10.3390/nano8110952>.
- [78] X. Zhang, Tea and cancer prevention, *J. Canc. Res. Updates* 4 (2) (2015) 65–73, <https://doi.org/10.6000/1929-2279.2015.04.02.4>.
- [79] Y. Yang, P. Jin, X. Zhang, N. Ravichandran, H. Ying, C. Yu, H. Ying, Y. Xu, J. Yin, K. Wang, M. Wu, Q. Du, New epigallocatechin gallate (EGCG) nanocomplexes co-assembled with 3-mercapto-1-hexanol and  $\beta$ -lactoglobulin for improvement of antitumor activity, *J. Biomed. Nanotechnol.* 13 (7) (2017) 805–814, <https://doi.org/10.1166/jbn.2017.2400>.
- [80] Y. Niu, F. Stadler, T. He, X. Zhang, Y. Yu, S. Chen, Smart multifunctional polyurethane microcapsules for the quick release of anticancer drugs in BGC 823 and HeLa tumor cells, *J. Mater. Chem. B* 5 (48) (2017) 9477–9481, <https://doi.org/10.1039/C7TB02570J>.
- [81] X. Zhang, Ultrasonication assisted Layer-by-Layer technology for the preparation of multi-functional anticancer drugs paclitaxel and lapatinib, 2013. <https://ui.adsabs.harvard.edu/abs/2013PhDT28Z>.
- [82] J. Ouyang, X. Ji, X. Zhang, C. Feng, Z. Tang, N. Kong, A. Xie, J. Wang, X. Sui, L. Deng, Y. Liu, W. Tao, In situ sprayed NIR-responsive, analgesic black phosphorus-based gel for diabetic ulcer treatment, *Proc. Natl. Acad. Sci. U.S.A.* (2020) 202016268, <https://doi.org/10.1073/pnas.2016268117>.
- [83] Z. Tang, X. Zhang, Y. Shu, M. Guo, H. Zhang, W. Tao, Insights from nanotechnology in COVID-19 treatment, *Nano Today* 36 (2020) 101019, <https://doi.org/10.1016/j.nantod.2020.101019>.
- [84] Z. Yang, D. Gao, X. Guo, L. Jin, J. Zheng, Y. Wang, S. Chen, X. Zheng, L. Zeng, M. Guo, X. Zhang, Z. Tian, Fighting immune cold and reprogramming immunosuppressive tumor microenvironment with red blood cell membrane-camouflaged nanobullets, *ACS Nano* (2020), 1936–0851, <https://doi.org/10.1021/acsnano.0c07721>.